J. Fluid Mech. (2014), *vol.* 750, *pp.* 284–315. © Cambridge University Press 2014
doi:10.1017/jfm.2014.256

The role of conservative forces in rotor aerodynamics

G. A. M. van Kuik[1],†, D. Micallef[2], I. Herraez[3], A. H. van Zuijlen[1] and D. Ragni[1]

[1]Faculty of Aerospace Engineering, Technical University Delft, Kluyverweg 1, 2629HS Delft, The Netherlands

[2]Department of Mechanical Engineering, Faculty of Engineering, University of Malta, Msida MSD 2080, Malta

[3]ForWind, Carl von Ossietzky Universität Oldenburg, Ammerländer Heerstrasse 136, 26129 Oldenburg, Germany

(Received 11 September 2013; revised 17 February 2014; accepted 4 May 2014; first published online 9 June 2014)

The theory to predict the performance and loads on rotors (propellers, screws, windmills) has a history of more than a century. Apart from modern computational fluid dynamics and vortex panel models taking the true blade geometry into account, most other models proceed from an infinitely thin actuator disc or line. These models assume an externally defined force field distributed at the disc or line, representing the loads on the real rotor. Given this force field, the flow is solved by momentum balances or by the equations of motion. The use of external force fields was discussed in textbooks of the first decades of the 20th century, but has received little attention since then. This paper investigates the higher-order effect of adding thickness to the actuator disc or changing the actuator line to a blade with cross-sectional dimensions. For the generation of a Rankine vortex by a force field acting on an actuator disc with thickness, an exact solution has been found in which not only the thrust and torque determine the flow, but also a radial force. This force is conservative, in contrast to the other force components. For rotor blades, a conservative normal and radial force acting on the chordwise bound vorticity is present. This explains the experimentally observed inboard motion of the tip vortex of model wind turbine rotors before the wake induction field drives it outboard. Simulations by computational fluid mechanics and a vortex panel code reproduce the inboard motion, but an actuator line analysis, in which the chordwise vorticity is absent, does not. The conservative load is only 1–2 % of the thrust on the entire blade but ≈10 % of the thrust at the tip ($r/R > 0.9$). Conservative forces at the disc and rotor blade vanish for vanishing disc thickness or blade cross-section, so play no role in any of the infinitely thin actuator disc or line methods. However, if higher-order effects of non-zero dimensions are to be modelled, the conservative force field has to be included.

Key words: general fluid mechanics, vortex interactions, wakes

---

† Email address for correspondence: g.a.m.vankuik@tudelft.nl

1. Introduction

1.1. *Brief history of rotor aerodynamics*

The actuator disc is the earliest model for any rotor in fluid dynamic calculations: a permeable disc with a uniform pressure jump represents a rotor with an infinite number of blades. The classical momentum theory started with the work of Rankine (1865), who defined the concept of a stream tube and the actuator disc, and Froude (1889), who formulated that the velocity through the disc is the average of the velocity far upstream and far downstream in the wake. Lanchester (1915) was close to finding the optimal performance of a static propeller and a wind turbine with a uniform axial load distribution, but he did not continue on Froude's result. A firm assessment of the ideal performance of the static propeller was first obtained by Joukowsky (1918). Two years later Betz (1919) and Joukowsky (1920) derived the ideal performance of a wind turbine at the same time (see van Kuik 2007; Okulov & van Kuik 2012). Since then, the actuator disc concept has been adapted so as to make it useful for rotors with a finite number of blades. Glauert (1935, chapter III) coupled disc loads to blade loads and introduced the torque in the momentum theory, resulting in the blade element momentum (BEM) method, which is still the basis for most rotor design codes. Furthermore Glauert (1926) added the first correction for discs representing heavily loaded wind turbines. The main problems that were left after Glauert's work were the refinement of the blade model and the adaptation of the BEM method to off-design conditions. Much effort has been spent in making the BEM method suitable for the real rotors of helicopters and wind turbines, by introducing models for three-dimensional flow along the blade surface, blade deformations, tip effects, yawed flow, dynamic inflow, unsteady aerofoil behaviour and dynamic stall, wind shear, atmospheric turbulence, etc. Helicopter and wind energy textbooks such as Leishman (2000), Burton *et al.* (2001) and Manwell, McGowan & Rogers (2007) present surveys of these BEM adaptations, although improved corrections are continuously being published, up to Shen *et al.* (2005) and Madsen *et al.* (2010).

Besides momentum theory, also vortex theory is used to model the action of an N-bladed rotor. Joukowsky (1912–1918) and Betz (1920) formulated conditions for the optimal rotor. Both assumed a linearized solution (a wake with constant radius), but used a different model for the vorticity shed by the blades. Goldstein (1929) solved Betz's model for two, three and four blades. With the current knowledge on vorticity dynamics, Okulov & Sørensen (2010) compared both conceptual models quantitatively, and obtained results for increasing N. Some years earlier Breslin & Andersen (1994) presented, besides the actuator disc theory, a thorough treatment of the lifting line theory and propeller design optimization. Modern computer power has enabled vortex lattice methods like that described by Micallef *et al.* (2013), where boundary conditions are applied at the true blade surface. The potential flow solution provides details of the wake as well as the blade loads. Full solutions including viscous effects using computational fluid dynamics (CFD) are presented by many authors (e.g. Madsen *et al.* 2010; Sibuet Watters & Masson 2010; Troldborg, Sørensen & Mikkelsen 2010). Since the calculation time required for a complete solution of blade and wake flow is still too long, the blade is often represented by an actuator line as first proposed by Sørensen & Shen (2002). The blade is represented by a prescribed load distributed along a line replacing the blade (see e.g. Shives & Crawford 2013; Réthoré *et al.* 2014). A review of propeller aerodynamics is presented by Wald (2006) and similarly of CFD methods applied to wind turbine wakes by Sanderse, van der Pijl & Koren (2011).

Despite the progress in blade aerodynamics, the actuator disc has received and is still receiving continual attention. Wu (1962) derived a differential equation describing the flow in terms of the stream function, the circulation around the axis and the component of the disc load perpendicular to the stream tube. When the disc has a uniform normal load, the wake is bounded by a vortex sheet and the wake flow itself is free of vorticity. This enables one to rewrite Wu's equation as a potential flow, after which calculations determine the position and strength of the vortex sheet. Greenberg (1972) published results for the uniformly loaded disc. Øye (1990) and Mikkelsen *et al.* (2009) represented the vortex sheet emanating from the edge of a uniformly loaded disc by a series of concentric vortex rings. The strength and position of these rings are calculated with the appropriate boundary conditions. Sørensen & van Kuik (2011) presented an extension to Glauert's theory for rotating disc force fields including torque when the rotational speed tends to zero. Conway (1995) presented analytical solutions for the linearized flow field, which was extended to exact analytical solutions for non-uniform load distributions in inviscid flow in Conway (1998). His results have become a benchmark to test other flow solvers. Rosen & Gur (2008) also developed a semi-analytical actuator disc model, in which the disc is represented by a distribution of sinks. They found a close correspondence with Conway's results. Also Réthoré *et al.* (2014) used Conway's work to successfully validate a CFD actuator disc method. A first CFD calculation for many actuator disc flow states is presented by Sørensen, Shen & Munduate (1998). An example of the calculation of the hover flow state is published by Spalart (2003).

This brief representation of the state of the art in rotor aerodynamics shows that it has a long history with a well-developed foundation in analytical theory, vorticity and CFD models as well as design methods. In some of the models and methods, the blade is replaced by its force field, in order to simplify the model and accelerate the calculations. What is underexposed in the literature discussed here is what the requirements are for this force field to accurately represent the blade load. Wald (2006, § 3.4) discusses the flow singularity at the edge of an infinitely thin blade, creating an edge force. He shows in his figure 5 the outer part of a blade having bound vorticity in radial as well as chordwise direction. For such curved lines of vorticity Milne-Thomson (1966, § 10.61) discusses the occurrence of in-plane Kutta–Joukowsky forces resulting from self-induction. These effects are not accounted for in actuator line, lifting line or BEM models. The research presented here is on these aspects of a force field representing an actuator disc or a rotor blade.

Actuator discs are also used to model devices in flows that are restricted laterally by walls, e.g. tubes. The flows are treated by Horlock (1978) and are outside the scope of the present paper.

1.2. *The use of external force fields in fluid dynamics*

Except for the vortex lattice models and the CFD models based on real surface boundary conditions, all the methods discussed above prescribe the force field as input in the flow solver. The question of how to determine the force fields is solved either by the definition of the problem (in actuator disc analyses: based on physical arguments, a load distribution is assumed (see Sørensen *et al.* 1998)) or by iteration with other methods (in actuator line and momentum analyses: for a given flow field, the load is taken from a blade element calculation, which is used as force input in the calculation of an updated flow field (see Shen, Zhu & Sørensen 2012)). In all cases these forces contribute to the conversion of power, so these are classified as non-conservative forces.

The use of external force fields is discussed in old papers and textbooks, such as von Kármán & Burgers (1935), but is in contrast to most fluid dynamic analyses where the force field (or pressure distribution) is output instead of input. However, particularly in rotor aerodynamics, the use of predefined force fields has some advantages. It allows for much easier physical interpretation of flow problems, since the thrust, being the integrated load, is the main parameter defining flow states.

The question addressed in this paper is whether the force field used in the classical actuator disc theory, BEM design methods and actuator line analyses is fully consistent with the force field or pressure distribution that would follow from a full CFD or vortex lattice method, from experiments or, if present, from a complete analytical solution. The motivation for this question is twofold. First is an exact solution of Wu's equation, to be discussed in § 3.4, where a radial component of the disc load is present when the disc has thickness. Second, analyses of several wind tunnel experiments (Xiao *et al.* 2011; Micallef 2012; Micallef *et al.* 2012) have shown details of the flow field very close to the tips of model wind turbine rotor blades for which only radial pressure gradients or loads at the blade tip provide an explanation: after being released by the blade tip, the tip vortex first moves inboard before the wake expansion drives it outboard. The inboard motion leads one to expect a similar radial load.

In contrast to the components of the load contributing to the thrust and torque, a radial load is conservative since it does not contribute to the power conversion. The rotor and disc analyses discussed in § 1.1 make no distinction between conservative and non-conservative loads, and do not model a radial load. It is expected that, if there is an effect of radial loads, it will be a higher-order effect having little impact on the overall loads. However, higher-order effects may help to improve the prediction of the tip vortex trajectory close to the tip, which in turn may have additional advantages for tip geometry design and associated aeroacoustic effects.

The analysis builds on previous work on actuator discs and rotors. In van Kuik (2012) the limit transitions required to convert a rotor into a disc are analysed. When the rotor is represented by its force field, the limit transitions, like the number of blades going to infinity, turn this force field into the well-known uniform pressure jump across the disc as modelled by the founders of modern rotor theory, Joukowsky (1912–1918) and Betz (1920). Van Kuik (2014) compares the conservation of vorticity in the disc and rotor flows. The force field of a disc is known to generate vorticity, while the bound and wake vorticity of a rotor blade constitute a system in which the circulation is conserved. It is shown that this is an apparent distinction since both flows generate vorticity while the circulation is conserved.

1.3. *Objective and outline*

The distinction between conservative and non-conservative forces and the role of both in actuator disc and rotor flows is investigated. The research questions are as follows:

(*a*) Which part of the load on a rotor blade and actuator disc is conservative or non-conservative? What is the physical origin of both? And what effect may the conservative force have on the flow and performance of rotors?

(*b*) If the conservative force is demonstrated to play a role in the rotor aerodynamics, is this accounted for by state-of-the art rotor aerodynamic design and analysis methods?

In the next section the distinctive properties of conservative and non-conservative forces are analysed, after which two examples of a flow with a conservative force are treated. Section 3 presents an exact analytic solution of the stream-tube equation for the disc developed by Wu (1962). The force field acting at a rotor blade is analysed in § 4. Finally, § 5 connects the disc and rotor analyses, evaluates the results with respect to the research objective and presents the main conclusions.

2. (Non-)conservative force fields in the Euler equation

The flow is assumed to be incompressible, inviscid and isentropic, so the Euler equation

$$\rho\frac{\partial \boldsymbol{v}}{\partial t}+\rho(\boldsymbol{v}\boldsymbol{\cdot}\nabla)\boldsymbol{v}=-\nabla p+\boldsymbol{f} \tag{2.1}$$

is valid as well as the continuity equation

$$\nabla\boldsymbol{\cdot}\boldsymbol{v}=0, \tag{2.2}$$

with $\boldsymbol{v}$ being the velocity vector (m s^{-1}), ρ the flow density (kg m^{-3}), p the pressure (N m^{-2}) and $\boldsymbol{f}$ the force density, volume force or force field (N m^{-3}). Rewriting (2.1) with the vector identity $(\boldsymbol{v}\boldsymbol{\cdot}\nabla)\boldsymbol{v}=\nabla(\boldsymbol{v}\boldsymbol{\cdot}\boldsymbol{v})/2-\boldsymbol{v}\times\boldsymbol{\omega}$ yields

$$\nabla H=\boldsymbol{f}-\rho\frac{\partial \boldsymbol{v}}{\partial t}+\rho\boldsymbol{v}\times\boldsymbol{\omega}, \tag{2.3}$$

where H is the Bernoulli constant $p+\rho/2\boldsymbol{v}\boldsymbol{\cdot}\boldsymbol{v}$, and $\boldsymbol{\omega}$ the vorticity (rad s^{-1}).

The cylindrical coordinate system $(x,\ r,\ \varphi)$ is used, with the disc centreline coinciding with the positive x axis and with $\boldsymbol{e}$ denoting the unit vector with an appropriate index, as well as the local coordinate system (s, n, φ); see figure 1. The coordinate s is in the meridional plane tangent to the stream tube, and n is normal to the stream tube. Besides these inertial coordinate systems, also the rotating system $(x, r, \varphi)_{rot}$ is used, rotating with respect to the inertial system with the angular velocity $\varOmega$ (rad s^{-1}) of the force field. The velocity and vorticity in the inertial and rotating systems are related by

$$\begin{aligned} \boldsymbol{v}_{rot} &= \boldsymbol{v}-\boldsymbol{e}_{\varphi}\varOmega r, && (2.4)\\ \boldsymbol{\omega}_{rot} &= \boldsymbol{\omega}-2\boldsymbol{e}_{x}\varOmega. && (2.5) \end{aligned}$$

Only flows that are steady with respect to the rotating system are considered. For the axisymmetric disc in § 3, the flow is also steady in the inertial frame. For the rotor in § 4, the flow in the inertial system is unsteady but periodic.

The use of the force field $\boldsymbol{f}$ is discussed in old textbooks and papers, such as Prandtl (1918) and von Kármán & Burgers (1935), without making an explicit distinction between conservative and non-conservative components. Most modern textbooks pay some attention to the force term but at some moment assume that $\boldsymbol{f}$ is conservative, like the gravity force field. Here this assumption is not made but instead force fields are assumed to be confined to thin surfaces. When the surface has thickness ϵ, integration along the normal n_{ϵ} gives the surface load $\boldsymbol{F}$ (N m^{-2}):

$$\boldsymbol{F}=\int_{\epsilon}\boldsymbol{f}\,\mathrm{d}n_{\epsilon}. \tag{2.6}$$

More integrations result in a line force (N m^{-1}) or a discrete force (N), which will be named after its function, e.g. lift or thrust.

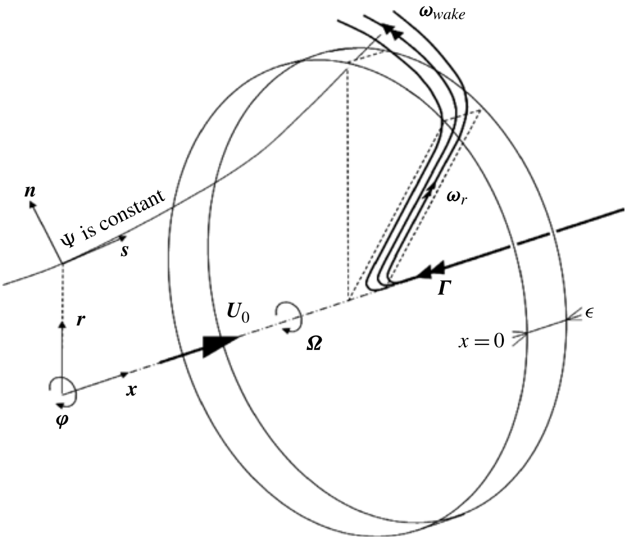

FIGURE 1. The vortex system of the actuator disc. Shown is the disc decelerating the flow. All vectors are in positive direction, except Γ_{axis} and ω_φ.

In general, the force field can have a non-conservative as well as a conservative component. A non-conservative $\boldsymbol{f}$ satisfies $\nabla \times \boldsymbol{f} \neq 0$, and is able to generate vorticity as shown by the curl of (2.3) (see Saffman 1992, pp. 10–11):

$$\frac{1}{\rho} \nabla \times \boldsymbol{f}_{non\text{-}cons} = \frac{\mathrm{D}\boldsymbol{\omega}}{\mathrm{D}t} - (\boldsymbol{\omega} \cdot \nabla)\boldsymbol{v}, \tag{2.7}$$

with the last term denoting the change of vorticity due to stretching or tilting of already existing vortex filaments. When $\boldsymbol{f}$ is distributed on a thin surface of which the limit $\epsilon \to 0$ is taken, the gradients tangential to the surface do not vary across the thickness ϵ. Integration of $\nabla \times \boldsymbol{f}$ then gives

$$\lim_{\epsilon \to 0} \int_\epsilon \nabla \times \boldsymbol{f} \, \mathrm{d}n_\epsilon = \nabla \times \boldsymbol{F} = \frac{\mathrm{D}\boldsymbol{\gamma}}{\mathrm{D}t} - (\boldsymbol{\gamma} \cdot \nabla)\boldsymbol{v}, \tag{2.8}$$

where the vortex sheet strength $\boldsymbol{\gamma} = \int \boldsymbol{\omega} \, \mathrm{d}n_\epsilon$. In the case when $\boldsymbol{F}$ is normal to the surface S of a lifting body, integration of $\nabla \times \boldsymbol{F}$ on S yields

$$\iint_S \nabla \times \boldsymbol{F} \, \mathrm{d}S = 0, \tag{2.9}$$

since the integrand consists of the tangential derivatives of the normal load, yielding zero after integration on a closed contour. The combination of (2.8) and (2.9) shows that the net generation of vorticity by a lifting surface with a normal load is zero. Locally the production of vorticity can be non-zero since locally $\nabla \times \boldsymbol{F} \neq 0$, but this is accompanied by production of an equal amount of vorticity with opposite sign somewhere else at S. This is the force-field-based explanation of the fact that any lifting surface produces the same amount of positive and negative vorticity.

Since the generation of vorticity implies that fluid particles receive an angular speed, it is expected that (2.7) represents the differential balance of angular momentum like

(2.1) represents the differential linear momentum balance. In van Kuik (2014) a proof for this is presented in the two-dimensional plane as well as for the meridional plane of axisymmetric flows without swirl.

A second difference between conservative and non-conservative forces regards the conversion of power. A conservative force field satisfies $\nabla \times \boldsymbol{f} = 0$ or, equivalently,

$$\boldsymbol{f}_{cons} = -\nabla \mathscr{F}, \tag{2.10}$$

where $\mathscr{F}$ is the potential of $\boldsymbol{f}$. Batchelor (1970, pp. 138, 157) and Kundu (1990, p. 102) mention that $\mathscr{F}$ can be considered as the potential energy. Furthermore, Batchelor suggests that 'under certain conditions the pressure might play the part of a potential energy', which is examined here. With (2.10) the Euler equation (2.1) becomes

$$\rho \frac{\partial \boldsymbol{v}}{\partial t} + \rho(\boldsymbol{v} \cdot \nabla)\boldsymbol{v} = \boldsymbol{f}_{non\text{-}cons} - \nabla(p + \mathscr{F}). \tag{2.11}$$

If the surface is a stream surface with steady flow, so with $v_n = 0$, and with $\boldsymbol{f}_{non\text{-}cons} = 0$, integration of the component normal at the surface gives $\Delta(p + \mathscr{F}) = 0$ by which indeed the pressure p_{cons} induced by $\boldsymbol{f}_{cons}$ acts as its potential: $\mathscr{F} = -p_{cons}$. This is reflected in the work done by a force field. Batchelor (1970, p. 157) shows the work done by a distribution of volume forces. Rewritten for inviscid isentropic flow this becomes

$$\boldsymbol{f} \cdot \boldsymbol{v} = \frac{\rho}{2} \frac{\partial \|v\|^2}{\partial t} + (\boldsymbol{v} \cdot \nabla) H \tag{2.12}$$

or using (2.11)

$$\boldsymbol{f}_{non\text{-}cons} \cdot \boldsymbol{v} = \frac{\rho}{2} \frac{\partial \|v\|^2}{\partial t} + (\boldsymbol{v} \cdot \nabla)(H - p_{cons}). \tag{2.13}$$

For steady flows with only conservative forces $(H - p_{cons}) = (H + \mathscr{F}) = \text{const.}$ along a streamline. Batchelor interprets this as the total energy of a material element being constant for inviscid steady isentropic flows when only conservative forces act. Let V be a volume with surface S encompassing the area at which $\boldsymbol{f}$ is distributed. For the disc and rotor flows considered here, the unsteady terms are either zero or periodic, so vanish in the integration on V. This yields, using Gauss's theorem,

$$\iiint_V \boldsymbol{f}_{non\text{-}cons} \cdot \boldsymbol{v} \, \mathrm{d}V = \iint_S (H - p_{cons})(\boldsymbol{v} \cdot \boldsymbol{e}_{n,S}) \, \mathrm{d}S, \tag{2.14}$$

with $\boldsymbol{e}_{n,S}$ as unit vector normal to S. With the exception of § 3.4.1, all actuator disc and rotor force fields are distributed on surfaces with finite dimensions. When the distance of S to these surfaces goes to infinity, $p_{cons} \to 0$, by which (2.14) shows that the non-conservative force field does work expressed as the change of H times the cross-flow through S.

Summarizing, force fields in the Euler equation of motion may be distinguished by:

(*a*) non-conservative force fields that create vorticity and perform work,

(*b*) conservative force fields that change the pressure field but conserve the total energy of fluid elements.

To distinguish the two types of force fields, these properties are not unambiguous. The force field may be non-conservative locally, so generate vorticity locally according to (2.7) or (2.8), while the integrated force field may be conservative according to (2.9) without a net generation of vorticity. The criterion of performing work may give different results when changing from an inertial coordinate system, as used above, to a system moving with the lifting surface in which the force fields acting on it do not perform work.

Since the force fields considered in this paper are distributed at surfaces with limited thickness ϵ, the following sections proceed from the requirement $\nabla\times\boldsymbol{F}\neq 0$ to classify a force field as non-conservative.

3. The actuator disc

The actuator disc force field is defined on a disc with a constant thickness ϵ and radius R. The disc and the force field rotate with angular speed $\boldsymbol{\Omega}=\boldsymbol{e}_x\Omega$. The undisturbed parallel flow U_0 is aligned with the disc centreline as shown in figure 1. The force and flow field are assumed to be steady and axisymmetric, so all time and azimuthal derivatives are zero.

3.1. *Power conversion*

The power produced or absorbed by an annulus dr of the actuator disc can be expressed in two ways: first as torque Q times rotational speed Ω, giving $\Omega\,\mathrm{d}Q=2\pi\Omega f_\varphi r^2\,\mathrm{d}r$; second by integration of (2.12) on the annulus, resulting in $2\pi r(\boldsymbol{v}\boldsymbol{\cdot}\nabla)H\,\mathrm{d}r$. Comparison shows that

$$\boldsymbol{f}\boldsymbol{\cdot}\boldsymbol{v}=\Omega r f_\varphi=(\boldsymbol{v}\boldsymbol{\cdot}\nabla)H. \tag{3.1}$$

The expression for f_φ is derived from the φ-component of (2.3):

$$f_\varphi=-\rho v_s\omega_n. \tag{3.2}$$

Since the flow is axisymmetric, the expression for the vorticity $\boldsymbol{\omega}$ is

$$\boldsymbol{\omega}=\boldsymbol{e}_s\frac{\partial(rv_\varphi)}{r\partial n}-\boldsymbol{e}_n\frac{\partial v_\varphi}{\partial s}+\boldsymbol{e}_\varphi\left(\frac{\partial v_n}{\partial s}-\frac{\partial v_s}{\partial n}\right), \tag{3.3}$$

so ω_n is a function of v_φ only. Herewith (3.1) becomes

$$\boldsymbol{f}\boldsymbol{\cdot}\boldsymbol{v}=\rho(\boldsymbol{v}\boldsymbol{\cdot}\nabla)(\Omega r v_\varphi)=\rho(\boldsymbol{v}\boldsymbol{\cdot}\nabla)\frac{\Omega\Gamma}{2\pi}, \tag{3.4}$$

where Γ denotes the circulation around the disc axis, $\Gamma=2\pi r v_\varphi$. The combination of (3.1) and (3.4) yields

$$\rho(\boldsymbol{v}\boldsymbol{\cdot}\nabla)\frac{\Omega\Gamma}{2\pi}=(\boldsymbol{v}\boldsymbol{\cdot}\nabla)H, \tag{3.5}$$

giving, with the assumption that $\|\boldsymbol{v}\|\neq 0$,

$$\frac{1}{\rho}(H-H_0)=\Omega\frac{\Gamma}{2\pi}=\Omega r v_\varphi, \tag{3.6}$$

where H_0 is the undisturbed value. This relation between converted power and azimuthal velocity has been obtained by Thwaites (1960, p. 473) and de Vries (1979, appendix C2). Expressed in terms of vorticity, using (3.3), this power conversion equation becomes

$$\frac{1}{\rho}\nabla H=\Omega\nabla(rv_{\varphi})=\boldsymbol{e}_{\varphi}\Omega r\times\boldsymbol{\omega}. \tag{3.7}$$

Finally (3.4) is integrated on the disc volume to obtain the total power converted by the disc force field,

$$P=\rho 2\pi\Omega\iint(\boldsymbol{v}\boldsymbol{\cdot}\nabla)(rv_{\varphi})r\,\mathrm{d}r\,\mathrm{d}x, \tag{3.8}$$

which shows that this equals the increase of angular momentum given to the flow times the rotational speed.

3.2. *Conservative and non-conservative disc force fields*

Substitution of (3.7) in the Euler equation (2.3) leads to an equation with only kinematical terms:

$$\frac{1}{\rho}\boldsymbol{f}=-\boldsymbol{v}\times\boldsymbol{\omega}+\boldsymbol{e}_{\varphi}\Omega r\times\boldsymbol{\omega}. \tag{3.9}$$

An alternative expression for (3.9) in the rotating reference system is, using (2.4) and (2.5),

$$\frac{1}{\rho}\boldsymbol{f}=-\boldsymbol{v}_{rot}\times\boldsymbol{\omega}_{rot}+\boldsymbol{v}_{rot}\times 2\boldsymbol{\Omega}, \tag{3.10}$$

but the mixed expression

$$\boldsymbol{f}=-\rho\boldsymbol{v}_{rot}\times\boldsymbol{\omega} \tag{3.11}$$

is simplest. This is a general equation of motion for the actuator disc converting power, first presented in van Kuik & van Zuylen (2009). The subscript $_{rot}$ in (3.11) distinguishes it from the expression of a Kutta–Joukowsky force: the disc load is the cross-product of the velocity as experienced in the rotating system with the vorticity in the inertial system. Since it is expressed in kinematical terms, it enables an easier physical interpretation of the relation between loads and vorticity than when using the Euler equation including H.

An alternative way to derive (3.11) is to use the Euler equation (2.3) in the rotating reference frame, including the fictitious centrifugal and Coriolis force fields (see Batchelor 1970, p. 162),

$$\frac{1}{\rho}\nabla H_{rot}=\frac{1}{\rho}\boldsymbol{f}+\boldsymbol{v}_{rot}\times\boldsymbol{\omega}_{rot}+\boldsymbol{v}_{rot}\times 2\boldsymbol{\Omega}-\boldsymbol{\Omega}\times(\boldsymbol{\Omega}\times\boldsymbol{e}_r r), \tag{3.12}$$

and to evaluate the left-hand side, using (3.7), as

$$\begin{aligned}\frac{1}{\rho}\nabla H_{rot} &= \nabla\left(\frac{1}{\rho}H-v_{\varphi}\Omega r+\boldsymbol{e}_r\frac{(\Omega r)^2}{2}\right)\\ &= \boldsymbol{e}_r\Omega^2 r=-\boldsymbol{\Omega}\times(\boldsymbol{\Omega}\times\boldsymbol{e}_r r).\end{aligned} \tag{3.13}$$

It is apparent that the gradient of H_{rot} is the centripetal force balancing the centrifugal force, by which (3.12) becomes (3.10). The first term on the right-hand side of (3.10) is the Kutta–Joukowsky force on the bound vorticity, whereas the second term is the Coriolis force. Both are perpendicular to the local velocity, so do not perform work in the rotating system.

Evaluation of $\nabla \times \boldsymbol{f}$ in the (s, n, φ) coordinate system gives

$$\nabla \times \boldsymbol{f} = \boldsymbol{e}_s \frac{\partial (r f_\varphi)}{r \partial n} - \boldsymbol{e}_n \frac{\partial f_\varphi}{\partial s} + \boldsymbol{e}_\varphi \left(\frac{\partial f_n}{\partial s} - \frac{\partial f_s}{\partial n} \right), \tag{3.14}$$

which becomes after integration

$$\int_\epsilon \nabla \times \boldsymbol{f} \, \mathrm{d}s = \boldsymbol{e}_s \frac{\partial (r F_\varphi)}{r \partial n} - \boldsymbol{e}_\varphi \frac{\partial F_s}{\partial n}. \tag{3.15}$$

Since the normal derivatives are non-zero at the edge of the disc, any axisymmetric actuator disc loading has non-conservative components in the s and φ directions. The normal component is always conservative, since it cannot perform work as it does not contribute to the torque, and since it is absent in (3.15). Still, the load itself, $F_n = \int f_n \, \mathrm{d}s$, may be non-zero. Figure 1 shows that in the transition from bound radial vorticity to free wake vorticity the direction of $\boldsymbol{\omega}$ will gradually align with the direction of $\boldsymbol{v}_{rot}$, to be achieved at the downstream side of the disc. Consequently, $\boldsymbol{v}_{rot} \times \boldsymbol{\omega} \neq 0$ in the transition regions near the disc centre and edge, resulting in a load defined by (3.11):

$$\frac{1}{\rho} f_n = v_s \omega_\varphi - v_{\varphi,rot} \omega_s. \tag{3.16}$$

3.3. *Wu's actuator disc equation*

The actuator disc problem is treated thoroughly by Wu (1962). He considers an actuator disc placed normal to the undisturbed flow U_0, having an axisymmetric but otherwise arbitrary load distribution with an angular velocity Ω. Since the flow field induced by the force field is axisymmetric, it is possible to use the three-dimensional Stokes stream function ψ. Breslin & Andersen (1994) present an extensive discussion on Wu's equation, so here it suffices to say that it is the normal component of the Euler equation (2.3):

$$\frac{\partial H}{\partial n} = \boldsymbol{e}_n \cdot \boldsymbol{f} - \rho v_s \omega_\varphi + \rho v_\varphi \omega_s, \tag{3.17}$$

with all kinematical terms expressed in terms of ψ and Γ. Furthermore H is expressed in terms of Γ using (3.6), resulting in

$$\frac{\partial^2 \psi}{\partial x^2} + \frac{\partial^2 \psi}{\partial r^2} - \frac{1}{r} \frac{\partial \psi}{\partial r} = \frac{1}{2\pi} \frac{\partial \Gamma}{\partial \psi} \left(\Omega r^2 - \frac{\Gamma}{2\pi} \right) - \frac{r}{\rho} \frac{f_n}{v_s}. \tag{3.18}$$

The last term f_n is the same as (3.16), being a conservative force. Without the f_n term, (3.18) is known as the Bragg–Hawthorne equation, first published in Bragg & Hawthorne (1950).

3.4. *An exact solution: the generation of a Rankine vortex*

Wu (1962) suggests that f_n may be neglected, as he considers this to be the component of the axial force density normal to the stream tube. A significant value of f_n then requires a large radial velocity component at the disc, which is not present in general. An exact solution of Wu's equation is found below, in which the f_n term is a purely radial force density. The solution was first presented as an abstract in van Kuik & van Zuylen (2009).

3.4.1. *The force and flow field*

This solution of Wu's equation is a Rankine vortex with a vortex core $r \leqslant \delta$ rotating as a solid body, and a potential flow for $r > \delta$:

$$\left.\begin{aligned} \psi &= \tfrac{1}{2} U_0 r^2, \\ v_\varphi &= \begin{cases} g(x)\varOmega r, & r \leqslant \delta, \\ g(x)\varOmega \delta^2/r, & r > \delta, \end{cases} \\ g(x) &= \begin{cases} x/\epsilon, & 0 < x < \epsilon, \\ 1, & x \geqslant \epsilon, \\ 0, & x \leqslant 0. \end{cases} \end{aligned}\right\} \tag{3.19}$$

The Rankine vortex is generated at the disc with a linear increase of the swirl for $0 < x < \epsilon$ and is sketched in figure 2. The vorticity enclosed by the disc volume is derived by applying (3.3), with the notation $\boldsymbol{\omega} = [\omega_x, \omega_r, \omega_\varphi]$,

$$\boldsymbol{\omega} = \begin{bmatrix} 2\varOmega \dfrac{x}{\epsilon} \\ -\varOmega \dfrac{r}{\epsilon} \\ 0 \end{bmatrix}_{r \leqslant \delta}, \quad \boldsymbol{\omega} = \begin{bmatrix} 0 \\ -\varOmega \dfrac{\delta^2}{r\epsilon} \\ 0 \end{bmatrix}_{r > \delta}, \tag{3.20a,b}$$

which gives, after integration across the disc thickness, the vortex sheet strength $\boldsymbol{\gamma} = \int \boldsymbol{\omega} \, \mathrm{d}x$,

$$\boldsymbol{\gamma} = \begin{bmatrix} \varOmega \epsilon \\ -\varOmega r \\ 0 \end{bmatrix}_{r \leqslant \delta}, \quad \boldsymbol{\gamma} = \begin{bmatrix} 0 \\ -\varOmega \dfrac{\delta^2}{r} \\ 0 \end{bmatrix}_{r > \delta}. \tag{3.21a,b}$$

For the flow outside the disc volume, the solution (3.19) satisfies (3.18) as can be checked by substitution. At the disc itself, this substitution provides the expression for f_n, with $v_s = U_0$ and $\partial/\partial\varPsi = (rU_0)^{-1}\partial/\partial r$. It is clear that f_n is purely radial, so $f_n = f_r$. At the disc volume, f_φ is determined by (3.2) and f_x by (3.4). For $r > \delta$ this gives an expression for f_x that does not vanish for $r \to \infty$. Addition of a constant force field $f_x = -\rho(\varOmega\delta)^2/\epsilon$ for $0 \leqslant r < \infty$ has no impact on the flow, since it adds a constant pressure downstream of the disc. It is a conservative force field satisfying (2.10) with $\mathscr{F} = \rho(\varOmega\delta)^2 x/\epsilon$. The result is, in dimensionless form,

$$\frac{\boldsymbol{f}}{\rho\varOmega^2 r} = \begin{bmatrix} \dfrac{r^2 - \delta^2}{r\epsilon} - \dfrac{xr}{\epsilon^2} \\ \dfrac{2x}{\epsilon}\left(1 - \dfrac{x}{\epsilon}\right) \\ \dfrac{U_0}{\varOmega}\dfrac{1}{\epsilon} \end{bmatrix}_{r \leqslant \delta}, \quad \frac{\boldsymbol{f}}{\rho\varOmega^2 r} = \begin{bmatrix} -\dfrac{xr}{\epsilon^2}\left(\dfrac{\delta}{r}\right)^4 \\ 0 \\ \dfrac{U_0}{\varOmega r}\dfrac{\delta^2}{r\epsilon} \end{bmatrix}_{r > \delta}. \tag{3.22a,b}$$

The resultant expressions for the disc load F are obtained by integration of f across the thickness ϵ:

$$\frac{\boldsymbol{F}}{\rho(\varOmega r)^2} = \begin{bmatrix} \dfrac{1}{2} - \left(\dfrac{\delta}{r}\right)^2 \\ \dfrac{\epsilon}{3r} \\ \dfrac{U_0}{\varOmega r} \end{bmatrix}_{r \leqslant \delta}, \quad \frac{\boldsymbol{F}}{\rho(\varOmega r)^2} = \begin{bmatrix} -\dfrac{1}{2}\left(\dfrac{\delta}{r}\right)^4 \\ 0 \\ \dfrac{U_0}{\varOmega r}\left(\dfrac{\delta}{r}\right)^2 \end{bmatrix}_{r > \delta}. \tag{3.23a,b}$$

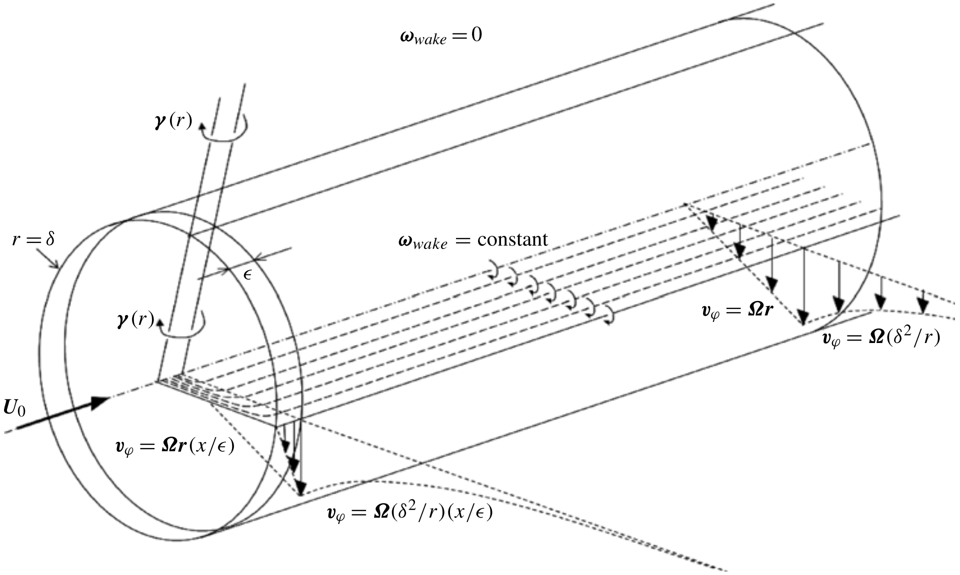

FIGURE 2. An exact solution of Wu's equation: the generation of a Rankine vortex, with core radius δ.

The solution satisfies the equation of motion (3.11), as is clear by substitution of (3.19) and (3.20) in (3.11). This returns (3.22), except for the conservative part of the force field $-\boldsymbol{\epsilon}_x \rho(\Omega\delta)^2/\epsilon$.

The loads F_x and F_φ are independent of the thickness ϵ; the load $F_{r,r>\delta} = 0$ but $F_{r,r<\delta}$ is $O(\epsilon)$, and contributes to the disc load when $\epsilon \neq 0$.

3.4.2. *Interpretation of the radial component of the load*

Inspection in the rotating frame of reference using (3.10) shows that f_r has a Kutta–Joukowsky as well as Coriolis part, with

$$f_{r,K\text{-}J} = 2\rho\left(1-\left(\frac{x}{\epsilon}\right)^2\right)\Omega^2 r, \tag{3.24}$$

$$f_{r,C} = -2\rho\left(1-\frac{x}{\epsilon}\right)\Omega^2 r. \tag{3.25}$$

In the inertial frame of reference, the radial pressure gradient is derived from the radial component of the Euler equation (2.1) with $v_r = 0$: $\rho v_\varphi^2/r = \partial p/\partial r - f_r$. Evaluation of $\rho v_\varphi^2/r$ with (3.19) gives

$$\begin{aligned}\frac{1}{\rho}\left(\frac{\partial p}{\partial r} - f_r\right) &= \Omega\frac{\partial(r v_\varphi)}{\partial r} - v_\varphi\frac{\partial v_\varphi}{\partial r}\\ &= \Omega^2 r g(x)(2-g(x)).\end{aligned} \tag{3.26}$$

In the wake $f_r = 0$ and $g = 1$, so $\rho^{-1}\partial p/\partial r = \Omega^2 r = v_\varphi^2/r$ satisfying the centripetal balance. This is not the case at the disc, where $g(x) = x/\epsilon$, resulting in the right-hand side of (3.26) being unequal to $\rho v_\varphi^2/r$. However, at the disc, f_r is non-zero, and substitution of f_r in (3.26) gives

$$\frac{1}{\rho}\frac{\partial p}{\partial r} = \Omega^2 r g^2(x) = \frac{v_\varphi^2}{r}, \tag{3.27}$$

which shows that the radial force density is required to restore the centripetal balance at the disc. This is in accordance with § 2, where it was demonstrated that a conservative force only changes the pressure field.

By (3.15) it is clear that F_x and F_φ are non-conservative, and F_r is conservative. Evaluation of (3.15) gives

$$\frac{1}{\rho}\int_\epsilon \nabla \times \boldsymbol{f}\,\mathrm{d}x = \boldsymbol{e}_x 2\Omega U_0 - \boldsymbol{e}_\varphi \Omega^2 r, \qquad r \leqslant \delta, \tag{3.28}$$

$$= -\boldsymbol{e}_\varphi \Omega^2 \frac{\delta^4}{r^3}, \qquad r > \delta, \tag{3.29}$$

which by inspection satisfies (2.7).

It is apparent that f_r is required to restore the centripetal balance at those positions in the actuator disc where the non-conservative force field creates vorticity that is convected downstream. Unlike f_x and f_φ, which behave as a Dirac delta function for $\epsilon \rightarrow 0$, f_r remains finite for vanishing thickness. The physical explanation is that both up- and downstream of the disc the pressure is independent of the thickness, by which the value of f_r required to maintain the centripetal balance at the disc has to be independent too.

3.4.3. *Numerical assessment of the impact of f_r*

The analytical solution shows that $f_r \neq 0$, but does not contribute to the disc load $F_r = \int f_r\,\mathrm{d}x$ when $\epsilon \rightarrow 0$ since f_r remains finite in this limit. The question whether omitting f_r is allowed in a flow calculation is still unanswered. To investigate this, the flow has been calculated with the CFD code 'Fluent' (see § B.1 for more information). The undisturbed flow has been set to $U_0 = \Omega\delta$. The thickness ϵ of the disc has been set to two values: $\epsilon = 0.05\delta$ and 1.0δ. The force density distribution (3.22) is applied, but once with and once without the radial force f_r. For the thin disc with $\epsilon = 0.05\delta$, the results with and without f_r are graphically almost indistinguishable, and are not shown here: both calculations give the flow field (3.19), so the radial load does not matter. For the thick disc with $\epsilon = \delta$, the results with and without f_r clearly show differences, as shown in figure 3. With the radial load included (see the upper row), the analytical solution is reproduced exactly, and downstream of the disc the flow does not change any more. In the absence of f_r, another flow field results, displayed in the lower row. The contrast with the analytical solution is observed in the wake, which is not fully developed immediately downstream of the disc, but is most visible in the plot of the radial velocity. The analytical solution gives $v_r = 0$ in the entire flow field, but v_r in the absence of f_r has a maximum value $v_r/U_0 \approx 0.07$.

In conclusion, the numerical analysis shows that F_x and F_φ do not define the flow uniquely. For the thick disc, F_r satisfying (3.22) needs to be added to reproduce the analytical solution, whereas $F_r = 0$ results in another flow solution with non-zero v_r. For thin discs $F_r = \int_\epsilon f_r\,\mathrm{d}x$ is negligible so it has no impact. Further interpretation of f_r and F_r is presented in § 5.1.

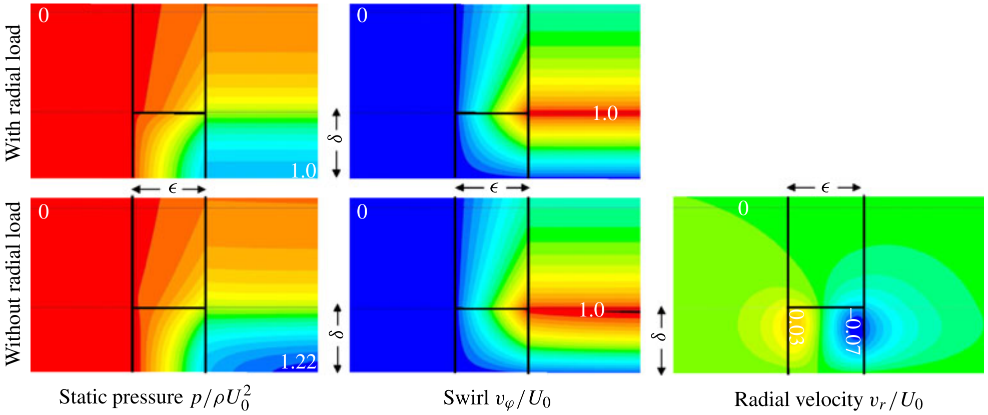

Static pressure $p/\rho U_0^2$ Swirl v_φ/U_0 Radial velocity v_r/U_0

FIGURE 3. (Colour online) The generation of a Rankine vortex flow by the force field (3.22) with and without f_r. Shown is the meridional plane with the undisturbed flow U_0 coming from the left. This disc is between the vertical lines. The kernel diameter δ equals the thickness ϵ. The radial velocity is not shown for $f_r = 0$ since $v_r = 0$ everywhere.

4. The rotor blade

Figure 4 shows the most simple rotor blade with a constant cross-section C, being a symmetric aerofoil without pitch or twist angle. This is not an optimal rotor design, but although not self-starting, it acts as a wind turbine rotor once $\Omega R/U_0$ is sufficiently high. In general, a tip aerofoil is cambered or has an inclination with respect to the disc plane, so the chordwise vorticity also has an axial component. By the chosen simple configuration, the blade can carry only radial and azimuthal vorticity components, which suffices for the present analysis. For rotors with non-zero axial vorticity, the analysis holds for the azimuthal part of the chordwise bound vorticity.

4.1. *Power conversion*

Expression (3.4) describes the local power conversion for the actuator disc. For the rotor, it is convenient to evaluate the azimuthally averaged power instead of the local power since the flow in the inertial system is periodic. The same line of arguments as in § 3.1 is followed. The power produced or absorbed at radius r is $2\pi \oint \boldsymbol{f} \boldsymbol{\cdot} \boldsymbol{v} r \, \mathrm{d}\varphi$, which equals the torque times the rotational speed in that annulus. With $\overline{\boldsymbol{f} \boldsymbol{\cdot} \boldsymbol{v}} = (1/(2\pi)) \oint \boldsymbol{f} \boldsymbol{\cdot} \boldsymbol{v} \, \mathrm{d}\varphi$ denoting the azimuthally averaged power at position r, this gives

$$\overline{\boldsymbol{f} \boldsymbol{\cdot} \boldsymbol{v}} = \rho \Omega r \overline{f_\varphi}. \tag{4.1}$$

For the unsteady rotor flow, the right-hand side of (4.1) is evaluated with the φ-component of (2.3):

$$f_\varphi = \frac{\partial H}{r \partial \varphi} - \frac{\partial v_\varphi}{\partial t} - \rho (v_x \omega_r - v_r \omega_x). \tag{4.2}$$

Since the flow is periodic, $\partial v_\varphi / \partial t$ and $\partial H/(r\partial\varphi)$ do not contribute to the azimuthal average of this component. With $\omega_x = 0$ it follows that

$$\overline{\boldsymbol{f} \boldsymbol{\cdot} \boldsymbol{v}} = -\rho \Omega r \, \overline{v_x \omega_r}. \tag{4.3}$$

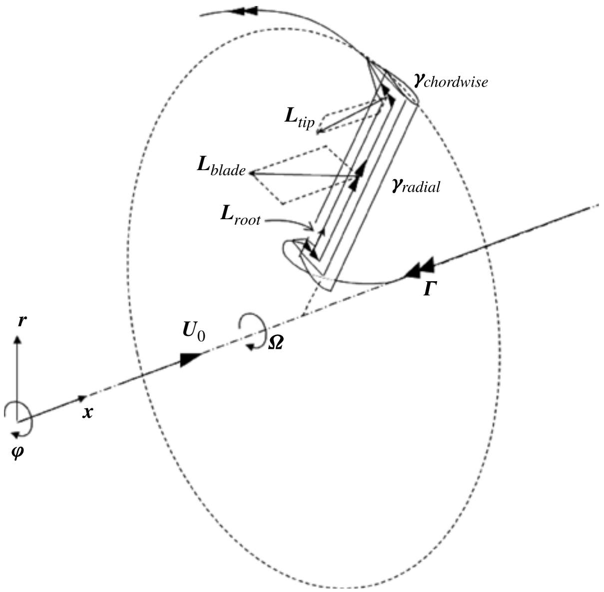

FIGURE 4. Rotor blade bound vorticity, with loads acting on the flow. The sign conventions are similar to those in figure 1. The loads are drawn assuming $v_x > 0$, $v_{\varphi,rot} < 0$, $v_r = 0$ near the root and $v_r < 0$ near the tip.

Using the complete expression for $\boldsymbol{\omega}$ instead of the axisymmetric equation (3.3), an equivalent result is obtained as in (3.4):

$$\overline{\boldsymbol{f}\cdot\boldsymbol{v}} = \rho\,\overline{(\boldsymbol{v}\cdot\nabla)(\Omega r v_\varphi)}. \tag{4.4}$$

The integrated power P becomes

$$P = \rho 2\pi\Omega \int_\epsilon \int_R \overline{(\boldsymbol{v}\cdot\nabla)(r v_\varphi)}\, r\,\mathrm{d}r\,\mathrm{d}x, \tag{4.5}$$

with the integration done across the blade thickness and from root to tip. For the disc as well as the rotor, the converted power is expressed as the rotational speed times the convective term $\rho(\boldsymbol{v}\cdot\nabla)(r v_\varphi)$, meaning the amount of angular momentum around the axis added to the flow.

4.2. *Conservative and non-conservative blade loads*

The expression (4.5) does not reveal which loads contribute to power conversion. Although the power can only be established in the inertial frame of reference since it is always zero in the rotating one, the loads are best analysed in the rotating frame of reference. The Euler equation in the rotating reference system is (3.12), written as $\boldsymbol{f} = \nabla H_{rot} - \rho \boldsymbol{v}_{rot} \times \boldsymbol{\omega}_{rot} - \rho \boldsymbol{v}_{rot} \times 2\boldsymbol{\Omega} + \rho\boldsymbol{\Omega} \times (\boldsymbol{\Omega} \times \boldsymbol{e}_r r)$. The two terms with $\boldsymbol{v}_{rot}$ are combined using (2.5), giving $\boldsymbol{v}_{rot} \times \boldsymbol{\omega}_{rot} + \boldsymbol{v}_{rot} \times 2\boldsymbol{\Omega} = \boldsymbol{v}_{rot} \times \boldsymbol{\omega}$. The lift $\boldsymbol{L}$ is obtained by integration of $\boldsymbol{f}$ across the blade cross-section C: $\boldsymbol{L} = \iint \boldsymbol{f}\,\mathrm{d}C$. The result is

$$\boldsymbol{L} = -\rho \iint_C \boldsymbol{v}_{rot} \times \boldsymbol{\omega}\,\mathrm{d}C + \iint_C \nabla(H_{rot} - \rho(\Omega r)^2)\,\mathrm{d}C. \tag{4.6}$$

In van Kuik (2012) it is shown that the axial and azimuthal components of the second integral are zero, but not necessarily the radial component. However, once integrated along the span, this term becomes zero too so this term is further omitted and the lift is

$$\boldsymbol{L} = -\rho \iint_C \boldsymbol{v}_{rot} \times \boldsymbol{e}_r \omega_r \,\mathrm{d}C - \rho \iint_C \boldsymbol{v}_{rot} \times \boldsymbol{e}_\varphi \omega_\varphi \,\mathrm{d}C. \tag{4.7}$$

The first integral gives the load on the radial vorticity, contributing to the rotor thrust and torque. The second integral in (4.10) is the lift on the azimuthal vorticity. Evaluated in the (s, n, φ) system using (2.4), $\boldsymbol{v}_{rot} \times \boldsymbol{e}_\varphi \omega_\varphi = \boldsymbol{v} \times \boldsymbol{e}_\varphi \omega_\varphi = -\boldsymbol{e}_n v_s \omega_\varphi$, so the integrated load is in the meridional plane normal to the stream tube, by which it is indicated as $\boldsymbol{L}_n$.

In order to distinguish conservative and non-conservative contributions to $\boldsymbol{L}$, the curl of it, $\iint \nabla \times \boldsymbol{f} \,\mathrm{d}C$, is evaluated in the (s, n, φ) system, giving

$$\iint_C \left[\boldsymbol{e}_s \left(\frac{\partial (r f_\varphi)}{r \partial n} - \frac{\partial f_n}{r \partial \varphi} \right) + \boldsymbol{e}_n \left(\frac{\partial f_s}{r \partial \varphi} - \frac{\partial f_\varphi}{\partial s} \right) + \boldsymbol{e}_\varphi \left(\frac{\partial f_n}{\partial s} - \frac{\partial f_s}{\partial n} \right) \right] r \,\mathrm{d}\varphi \,\mathrm{d}s. \tag{4.8}$$

Despite the fact that the derivatives with respect to φ and s are non-zero, they vanish after integration on the chord (respectively thickness), so

$$\nabla \times \boldsymbol{L} = \iint_C \left[\boldsymbol{e}_s \frac{\partial (r f_\varphi)}{r \partial n} - \boldsymbol{e}_\varphi \frac{\partial f_s}{\partial n} \right] \mathrm{d}C = \boldsymbol{e}_s \frac{\partial (r L_\varphi)}{r \partial n} - \boldsymbol{e}_\varphi \frac{\partial L_s}{\partial n}, \tag{4.9}$$

similar to (3.15). Load $\boldsymbol{L}_n$ is not included in (4.9) so is conservative, while the other components of $\boldsymbol{L}$ are non-conservative. Comparison of (4.7) and (4.9) leads to

$$\boldsymbol{L}_{non\text{-}cons} = -\rho \iint_C \boldsymbol{v}_{rot} \times \boldsymbol{e}_r \omega_r \,\mathrm{d}C, \tag{4.10}$$

$$\boldsymbol{L}_{cons} = \boldsymbol{L}_n = -\rho \iint_C \boldsymbol{v} \times \boldsymbol{e}_\varphi \omega_\varphi \,\mathrm{d}C. \tag{4.11}$$

The non-conservative part of $\boldsymbol{L}$ acts upon the spanwise or radial vorticity, while the conservative $\boldsymbol{L}_n$ acts upon the chordwise vorticity.

Both components of the vorticity are sketched in figure 4, where it is represented as a vortex sheet with strength $\boldsymbol{\gamma}$ resulting from the integration of the vorticity across the blade thickness. The relation between the two components is now expressed in terms of the circulation Γ. For any lifting surface, the well-known relation between the change of spanwise circulation and trailing vorticity is $\gamma_{chordwise} = -\partial \Gamma_{spanwise} / \partial r$, where r is the spanwise coordinate. Inspection of the derivation of this relation as presented by, for example, Lighthill (1986) shows that it also holds at the blade surface itself with $\Gamma_{spanwise}$ measured from the leading edge. Expressed in the coordinate system of figure 4 this becomes $\gamma_\varphi = \partial \Gamma_r / \partial r$, where the minus sign has vanished since the direction of the chordwise and azimuthal coordinates is opposite (see figure 5). The subscript r indicates that Γ is defined in a plane normal to a radius. Similarly, the circulation Γ_φ is defined in a plane normal to the chordwise direction. When measured from the tip to a local value of r then $\Gamma_\varphi(r) = -\int_R^r \gamma_\varphi \,\mathrm{d}\varrho$ or $\gamma_\varphi = -\partial \Gamma_\varphi / \partial r$. Combining the two expressions for γ_φ gives $\gamma_\varphi = \partial \Gamma_r / \partial r = -\partial \Gamma_\varphi / \partial r$ or

$$\frac{\partial (\Gamma_r + \Gamma_\varphi)}{\partial r} = 0. \tag{4.12}$$

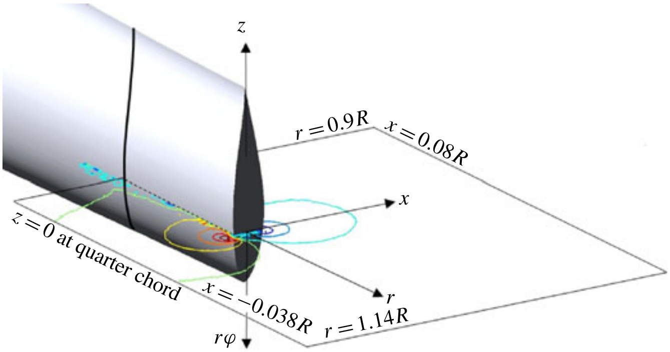

FIGURE 5. (Colour online) The geometry of the tip of the TUD-B rotor, the coordinate system and the plane at $z = 0$ coinciding with the quarter-chord position, used for the measurements and calculations. The iso-lines indicate the radial velocity. The square contour is used to determine the chordwise bound circulation (see § 4.3.3).

This gives the relation between the circulation around a radius and the circulation around an azimuthal line, at any position at the blade. It provides a coupling between the radial vorticity in (4.10) and the azimuthal vorticity in (4.11). For rotor blades having the circulation distributed along the span as constant as possible, the azimuthal vorticity will be located near the blade root and tip, so the conservative load (4.11) will then be concentrated near the root and tip.

The occurrence of the loads on the chordwise vorticity at the tip is known from measurements on helicopter and propeller model rotors. Grey *et al.* (1980) show the measured pressure distribution at the tip of a model rotor operating in hover, resulting in a significant increase of the normal force for $r/R > 0.98$. Ragni, van Oudheusden & Scarano (2011, 2012) report propeller-tip measurements using stereo particle image velocimetry (SPIV) and CFD calculations, showing details of the pressure distribution at the tip. A very good agreement between experimentally obtained and calculated tip pressure is shown, but no data for the integrated loads are given, although it is clear that the radial load is non-zero. The tip load effect is also known from translating wings, but it is noticeable only for non-slender wings. The additional normal load due to chordwise vorticity is described by, for example, Kűchemann (1984, p. 163). The additional in-plane or spanwise component of the load is less well known. Milne-Thomson (1966, § 10.61) pays attention to the in-plane component of the Kutta–Joukowsky load appearing when the lifting surface contains non-parallel vorticity lines. Because of the limited importance for wings, his analysis is restricted to the observation that the spanwise load is non-zero. In order to derive an order of magnitude of this spanwise load S, appendix A derives S for a wing with an elliptic planform. Load S is determined as the spanwise component of the Kutta–Joukowsky wing load, like the induced drag D is its component tangential to the flight path. The ratio $S/D = 2c_{max}/(\pi b)$, where c_{max} is the chord at mid-span, and b is the span. For an aspect ratio $b/c_{max} = 10$ and lift coefficient $C_L = 1$, the spanwise force on the half-wing is 1 % of the lift of the half-wing. It is clear that S is conservative, since it is perpendicular to the flight path and does not perform work. The physical origin of a possible radial load is the same as for the axial and azimuthal components: it is the blade surface pressure, now integrated on the radially projected surface.

The question whether it is important to include the load on chordwise vorticity in rotor design and analysis codes is still unanswered. This load is not taken into account in rotor design codes based on the BEM theory. These BEM codes use tip correction models as described in Shen *et al.* (2005), which incorporate information about the number of blades, tip speed ratio and tip geometry. The correction contains two constants that have been determined from experimental data. Vortex lattice and CFD codes that model the blade surface in sufficient detail automatically include the effect of chordwise vorticity. Recently several experiments on wind turbine model rotors using SPIV have provided many details of the flow around wind turbine blades. In the next section the results of one of these experiments are combined with analyses by a vortex panel and a CFD method. Emphasis is on assessing the occurrence of chordwise bound vorticity, determining the order of magnitude of the conservative load acting on it and the impact on the flow.

4.3. *Experimental and numerical results for a model wind turbine rotor*

4.3.1. *Inboard motion of tip vortex*

Akay *et al.* (2012), Micallef (2012) and Micallef *et al.* (2012, 2013) report experiments on two two-bladed rotors (TUD-A and -B) of 2 m diameter in the 3 m diameter Open Jet Facility of TU-Delft, with emphasis on the root and tip region. Schepers & Snel (2007) and Schepers, Boorsma & Munduate (2012) report experiments on a 4.5 m diameter three-bladed rotor called Mexico (Measurements and EXperiments In COntrolled conditions) in the $9.5 \times 9.5\ \mathrm{m}^2$ open test section of the German–Dutch Wind Tunnel. Xiao *et al.* (2011) report detailed tip vortex experiments on a 1.25 m diameter model of the NREL UAE phase VI wind turbine described by Hand *et al.* (2001), in an open test section of 3.2 m diameter. The flow near the blade tip of these rotors shows the tip vortex, when leaving the tip, moving inboard after which the wake expansion moves the vortex to a larger radius. Micallef *et al.* (2013) provide a detailed description of this phenomenon, Micallef (2012) and Micallef *et al.* (2012) give the experimental data of the TUD and Mexico rotor experiments and the analyses, as Xiao *et al.* (2011) does for the NREL model rotor. The first mention of this effect was by van Kuik (1991), where the physical mechanism is explained. The tendency of any tip vortex to first move inboard may be stronger than the wake expansion, depending on tip shape and tip load. For a propeller, both effects sum up, and the tip vortex always travels to a smaller radius.

The TUD-A rotor shows some inboard motion of the tip vortex, but this effect is better quantified for the other rotors. At 10° azimuth angle behind the blade quarter chord position, the radial position of the tip vortex of the Mexico rotor is $0.99R$, and of the TUD-B rotor $0.995R$ with the expansion to values $r > R$ starting only after 30° azimuth angle. The tip vortex of NREL-model rotor reaches $0.98R$ at 30° azimuth angle after which expansion starts. The inboard induction is caused by the chordwise vorticity at the tip, since all other blade bound or free wake vorticity components cannot induce such an inboard velocity, as becomes clear by qualitative considerations based on the Biot–Savart induction rules. Although the effect is least visible for the TUD-B rotor, it is most suited for detailed tip flow analysis because of its geometry and because the tip flow is measured in all required details. Figure 5 shows its almost cylindrical blade shape with a blunt tip surface having a zero pitch angle at $r = R$. All results concern the rotor operating at its optimal tip speed ratio seven at a wind speed of $6\ \mathrm{m\ s^{-1}}$. Appendix B.3 gives more details, including an assessment of the accuracy.

4.3.2. *Chordwise bound circulation*

CFD codes as used by Herraez *et al.* (2012) as well as vortex panel codes as used by Micallef *et al.* (2013) are able to capture the tip flow in detail. A summary of

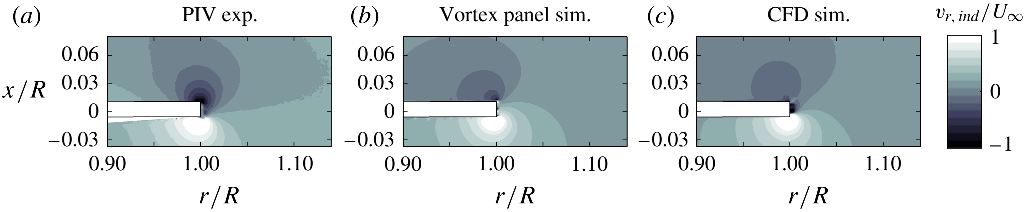

FIGURE 6. Comparison of the radial velocities in the meridional plane through the quarter-chord tip position; U_∞ is aligned with the rotor axis, and the tip speed ratio $\Omega R/U_\infty = 7$; see Micallef *et al.* (2011) for more details of the experiment.

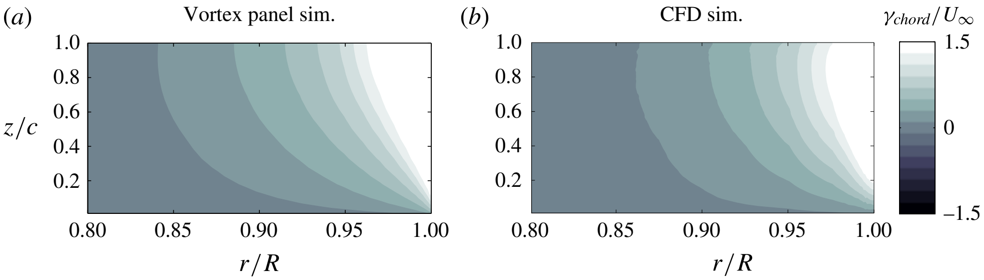

FIGURE 7. The chordwise vorticity determined by difference in radial velocities.

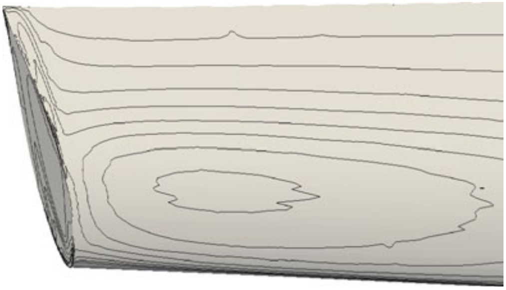

FIGURE 8. The pressure at the blade tip shown only qualitatively by isobars.

these codes is presented in § B.2. Figure 5 shows the plane of observation with the coordinate systems. Besides the (x, r, φ) system defined in figure 4, also the local (x, z, r) system is used since it is convenient to express local flow properties in the chordwise coordinate z. The measured and calculated radial flow are shown in figure 6. At the tip, a large difference in radial velocity at the pressure side of the blade tip ($x < 0$) and suction side is visible, indicating chordwise vorticity bounded at the tip. This vorticity component is shown in figure 7, indicating high values for $r/R > 0.97$. This chordwise vorticity may be considered as the beginning of the tip vortex. Figure 8 gives the pressure distribution at the suction side of the tip, showing for $r/R > 0.98$ the low-pressure region due to this vortex. Ferrer & Munduate (2007) show similar pressure distributions for other rotor lay-outs.

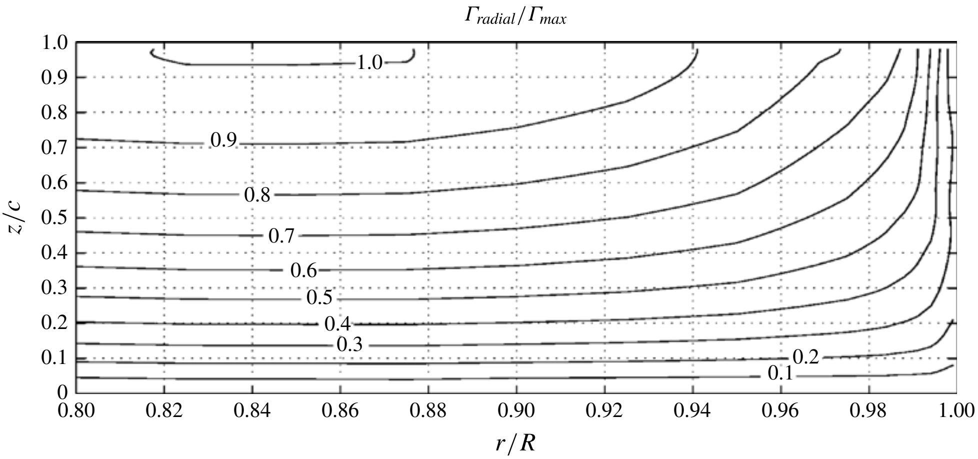

FIGURE 9. Iso-lines of constant percentage of the local circulation $\Gamma_r(r, z)/\Gamma_{r,max}(r)$ around the TUD-B rotor blade, determined by the CFD method; Γ_r is integrated from the leading edge to $\Gamma_r = \int_{le}^{z} \gamma_r \, d\zeta$.

Figure 9 shows how the blade bound radial vorticity γ_{radial} is connected to the bound chordwise vorticity γ_{chord} expressed in the circulation Γ. The value of the iso-circulation lines gives the local circulation, measured from the leading edge *le*, so $\Gamma_r(r, z) = \int_{le}^{z} \gamma_{radial} \, d\zeta$, divided by the maximum blade circulation. This maximum occurs at the trailing edge at $r/R = 0.825$. With Γ_φ replaced by $-\Gamma_z$, (4.12) gives $\Gamma_r - \Gamma_z = 0$ for a fixed chordwise position z when Γ_z is integrated inboard: $\Gamma_z(r, z) = \int_R^r \gamma_{chord} \, d\varrho$. Consequently the iso-lines give the value for Γ_r, measured along the chord from the leading edge, as well as Γ_z, measured along the radius from the tip to inboard. As an example at the trailing edge the spanwise circulation increases from 0 at $r = R$ to $\approx 0.9\Gamma_{r,max}$ at $r = 0.94R$. In other words, 90 % of the radial circulation leaves the blade as chordwise circulation in the outer 6 % of the blade. The figure shows that a small amount of the circulation leaves the tip – see the iso-lines 0.1 and 0.2. This missing part is not analysed further, but it is unbound vorticity or the contribution of the flat tip surface to the bound circulation. Figure 9 is similar to figure 5 of Wald (2006).

4.3.3. *The conservative tip load*

The chordwise circulation between $r = 0.9R$ and $r = R$, the normal force $\mathscr{N}$ and radial force $\mathscr{R}$ are determined by several means. Equation (4.11) gives the load on the chordwise vorticity for a certain radius, so integration along r gives the total load. This is approximated by the following procedure. The measured and CFD-calculated velocity field is integrated along the contour displayed in figure 5 to obtain the circulation $\Gamma(z)$ around the chordwise vorticity. The choice of the contour edges is such that no vorticity other than chordwise vorticity is contained within the integrated zone. On the contour side that cuts the blade, a linear jump in velocities is assumed, but this was found to have practically no influence on the calculated circulation. This procedure is repeated for six chordwise positions, with the results shown in figure 10. The two curves agree reasonably, with a maximum chordwise circulation of $\approx 0.9\Gamma_{radial,max}$. According to figure 9 the spanwise circulation at the trailing edge at $r/R = 0.9$ is $\approx 0.95\Gamma_{radial,max}$, which confirms the contour method.

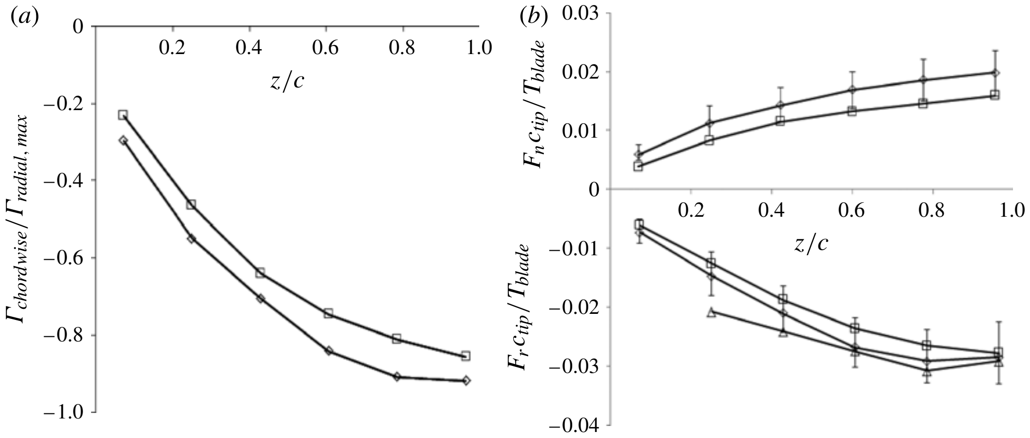

FIGURE 10. (*a*) Chordwise circulation, and (*b*) normal and radial loads. The squares show the K–J method applied to the CFD data. The diamonds indicate the same applied to the experimental data. The triangles present the experimental momentum method. The error bars for the K–J experimental load show the sensitivity for the position to determine $\boldsymbol{v}_{ref}$. The sensitivity of the radial load for variations of the contour in the momentum method is 5 % of the values indicated.

The force is calculated by chordwise integration of the Kutta–Joukowsky load $-\rho \boldsymbol{v}_{ref} \times \boldsymbol{\Gamma}$, where the equivalent velocity $\boldsymbol{v}_{ref}$ is the velocity in the (x, r) plane at a position close to the tip. The choice of this position is not straightforward, so when using the experimental data the sensitivity of the choice is assessed by determining $\boldsymbol{v}_{ref}$ at five positions: $(x/R, r/R) = (-0.04, 1.0)$, two positions with $\Delta r = \pm 0.02R$ and two with $\Delta x = -0.01R$ and $+0.015R$. The variation in the results is shown by the error bars in figure 10. When using the CFD data, for the same procedure, the position $(-0.04, 1.0)$ is used. Furthermore, the radial load is found by applying a radial momentum balance using the measured velocity field based on a contour as shown in figure 5, but with $r = R$ as inboard boundary instead of $r = 0.9R$. By doing so, the pressure at the flat tip surface is the source term in the balance giving the radial load. The sensitivity for the choice of the contour is checked by varying the position of the other contour sides. The momentum method is described in del Campo *et al.* (2013), where it is applied to determine the load on the radial circulation, with some more details given in § B.3.

The results of figure 10 are integrated along the chord to obtain the normal and radial load given in table 1. Furthermore, the loads as obtained by direct integration of the CFD-calculated pressure are given. The results agree reasonably well, with the pressure integrated radial load deviating most. The ratio of the radial force to the thrust of the blade has the same order of magnitude as the ratio of the spanwise force to the lift at one half of an elliptic wing calculated in appendix A: 1–2 %, so the contribution of the conservative tip loads to the overall rotor load is very small. However, when $\mathscr{N}$ and $\mathscr{R}$ are normalized by the thrust acting within the area of this research as defined in figure 5, the order of magnitude changes to 10 % of the thrust T_{tip} at the blade for $r > 0.9R$.

Besides the loads, also the tip vortex trajectories are compared. Figure 11 shows the calculated trajectories in comparison with the measured values. The CFD blade results corresponds to the CFD analysis discussed so far; the actuator line (CFD AL)

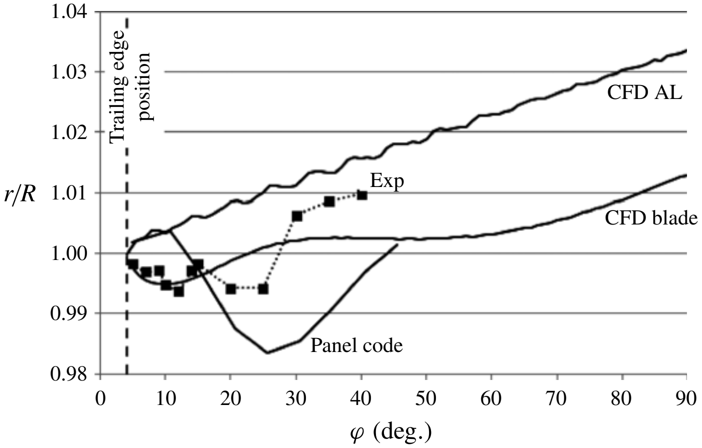

FIGURE 11. The radial coordinate of the tip vortex as a function of the azimuth angle measured from the $c/4$ position.

	CFD		Experiment	
	P	K–J	K–J	MOM
$\mathscr{N}$	1.2	1.0	1.3 ± 0.3	—
$-\mathscr{R}$	1.2	1.8	1.9 ± 0.4	2.2 ± 0.1

TABLE 1. The normal load $\mathscr{N}$ and the radial load $\mathscr{R}$ at the tip, as a percentage of T_{blade}. Here P, K–J and MOM refer to the pressure, Kutta–Joukowsky and momentum methods explained in § 4.3.3.

results are presented in the following section. Both CFD results are obtained by taking the average position of 100 streamlines forming the tip vortex. For the panel code, the trajectory is the vorticity filament that leaves the blade at the trailing edge of the tip. Although there are differences between the experimental data and calculated trajectories, the CFD blade and panel code results confirm that the tip vortex moves somewhat inboard before expansion starts after approximately 30° azimuth angle after the $c/4$ position.

4.4. *Comparison with simulations without chordwise vorticity*

In § 4 the impact of the conservative radial load on the flow was analysed by comparing numerical flow field solutions with and without the radial load. A similar comparison is done here, by comparing the previous CFD results with results obtained by an actuator line analysis using the same code. In an actuator line simulation, the blade is modelled as a line, so all chordwise information is lost like in a lifting line approach. A lifting line models the bound vortex representing the blade bound radial vorticity, whereas the actuator line carries the axial and azimuthal loads of the blade, concentrated at this line. The actuator line is the force field equivalent of the lifting line, and is used often in rotor aerodynamics. The actuator line analysis of this paper uses the same method as explained in Shen *et al.* (2012).

Since all chordwise information is discarded, the bound chordwise vorticity and the loads acting on it are absent. Figure 11 shows the comparison of the actuator line

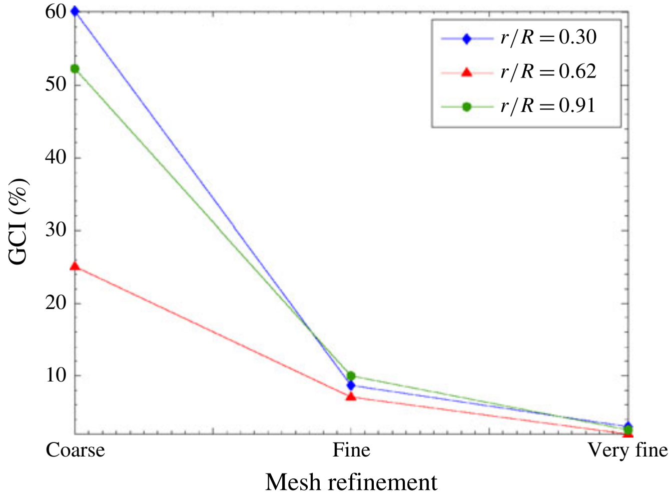

FIGURE 12. (Colour online) The GCI of the panel code for an increasingly finer mesh.

simulation (CFD AL) and the simulation for the blade (CFD blade), revealing a clear difference: the wake expansion in CFD AL starts immediately after the tip vortex is released, while this is delayed in CFD blade. The slope of the expansion is the same. When the expansion part of CFD blade is interpolated to $r = R$ keeping the same slope, the equivalent delay in wake expansion compared to CFD AL is 50° azimuth angle.

5. Interpretation of the results and conclusions

5.1. *Reflection on the role of conservative forces*

Although the disc flow in § 3 and rotor flow in § 4 are very different, the conservative part of the associated force fields show similar properties. In both cases, the conservative force changes the pressure field locally, as they do not influence the boundary conditions at large distances from where they act. The non-conservative forces do so as they perform work and create vorticity. However, conservative forces have an indirect effect on the far field since the modification of the pressure field changes the action of the non-conservative forces.

Conservative and non-conservative forces depend in essentially different ways on the geometry of the surface or volume carrying them. The non-conservative forces, like those contributing to thrust and torque, are determined by the radial bound circulation, which can be modelled by lifting line analyses. In such analyses, no geometrical information is necessary once the circulation is defined. In contrast to this, conservative forces do depend on geometry since they vanish for vanishing disc thickness or blade cross-section. Unlike non-conservative forces, they do not behave as a delta function for vanishing thickness or cross-section. This implies that the effect of the conservative forces is of higher order compared to the effect of non-conservative forces.

Since the conservative force field does not convert power nor produce vorticity, it may be discarded from the force field that induces the flow, without violating conservation laws or far-field boundary conditions. This was shown by the disc calculations without the radial force, and the actuator line calculations for the rotor. However, the resulting flow field differs from the 'original' flow field by this higher-order effect. For infinitely thin discs, or lifting/actuator line analyses, there is no difference with and without the conservative force.

The physical origin of the conservative force field is the same as of the non-conservative one, which is the pressure distribution at the rotor blade. When expressed as the load on bound vorticity, there is a clear distinction: in the flow cases studied here, the non-conservative load acts on radial bound vorticity, whereas the conservative load acts on axial disc bound vorticity, § 3, or azimuthal blade bound vorticity, § 4.

5.2. *Conclusions*

Here the two research questions defined in § 1.3 are answered:

(*a*) Force fields representing the action of lifting surfaces having non-zero thickness or chord can be distinguished by non-conservative forces creating vorticity and performing work, and conservative forces only changing the pressure field.

(*b*) The force density term in the actuator disc equation of Wu (1962) is shown to be a conservative force density. An exact solution, representing the generation of a Rankine vortex by a thick actuator disc, includes this force density, which becomes a radial load after integration across the disc thickness. This load is required to maintain the radial pressure gradient at the disc. A numerical analysis shows that the exact solution is not reproduced when the conservative radial load is not included. The conservative force depends linearly on the disc thickness, so disappears for an infinitely thin disc.

(*c*) A similar force acts on the chordwise bound vorticity of rotor blades, with a normal and radial component. This force is conservative, unlike the thrust and torque. For a model wind turbine rotor, the chordwise vorticity and the load have been identified by experimental and numerical analyses. The magnitude of the load is 1–2 % of the axial force per blade or ≈10 % of the axial force at the tip defined by $r > 0.9R$.

(*d*) The CFD and panel code analyses confirm the experimentally observed initial inboard motion of the tip vortex before wake expansion moves it to a larger radius. This happens ≈30° azimuth angle after the quarter-chord position of the blade tip. An actuator line analysis, which does not account for the conservative load, does not reproduce the inboard motion.

(*e*) The conservative component of the force field is taken into account by vortex lattice and CFD methods that model the rotor blade as a surface with dimensions.

(*f*) For lifting/actuator line models and analyses based on infinitely thin discs, like the exact solutions of Conway (1998), conservative forces play no role. These models/analyses are unaffected by the results presented here.

Acknowledgements

The authors thank John Conway of Agder University and Wen Zhong Shen of DTU for discussions on a very early version of § 3.4, and John Bye of the University of Melbourne for proof-reading. Many thanks go to the Hanse-Wissenschaftskolleg, which offered the first author a sabbatical leave to write this paper.

Appendix A. Spanwise load on an elliptic wing

The wing is placed in a Cartesian coordinate system with the span b ranging from $y = -b/2$ to $y = b/2$. The chord length has an elliptical distribution: $c(y)/c_{max} = \sqrt{(1-(2y/b)^2)}$. The undisturbed velocity U_0 is in the x direction with the positive

x pointing downstream and the z coordinate points upwards. The elliptic planform gives an elliptic distribution of the bound circulation $\Gamma(y)/\Gamma_{max} = \surd(1-(2y/b)^2)$, where Γ_{max} is the circulation around the wing at mid-span position. The velocity perpendicular to the undisturbed velocity, the downwash, is $v_z = -\Gamma_{max}/(2b)$. It is assumed that the vortex sheet emanating from the wing is in the x–y plane. The chordwise vorticity is given by $\gamma_c = -\mathrm{d}\Gamma/\mathrm{d}y$, so integration of the spanwise component of the Kutta–Joukowsky load on the surface A of the half-wing gives

$$S = -\rho \iint_A \boldsymbol{e}_y \boldsymbol{\cdot} \boldsymbol{v} \times \boldsymbol{\gamma}\, \mathrm{d}x\,\mathrm{d}y = -\rho \frac{\Gamma_{max}}{2b} \int_b c\, \mathrm{d}\Gamma \tag{A 1}$$

$$= -\frac{\rho}{4} \Gamma_{max}^2 \frac{c_{max}}{b}. \tag{A 2}$$

Comparison with the induced drag, $D = -\pi\rho/(8\Gamma_{max}^2)$, shows that the ratio $S/D = 2c_{max}/(b\pi)$. For an aspect ratio $b/c_{max} = 10$ and lift coefficient $C_L = 1$, the spanwise force on the half-wing is 6 % of the induced drag and 0.5 % of the lift of the entire wing.

Appendix B. The numerical and experimental methods

B.1. *Actuator disc calculations in* § *3*

The actuator disc calculations are performed with the finite volume solver Fluent 6.3.26. The configuration models two-dimensional axisymmetric inviscid incompressible flow with swirl, hence resolving the incompressible Euler equations (2.1) and (2.2). The actuator disc is modelled with a core radius $\delta = 1$ m and thickness ϵ. Two cases are considered, one with $\epsilon = 0.1\delta$ and one with $\epsilon = \delta$. The total domain size extends 10δ upstream of the disc, 45δ downstream and 25δ in the radial direction from the axis of symmetry. The disc itself is discretized uniformly with quadrilateral cells and enclosed by a region with quadrilateral cells extending 1.5δ upstream and 5δ downstream of the disc and 2.5δ in the radial direction. The rest of the domain is discretized with triangular cells. In both cases the total number of cells adds up to approximately 440 100. Although steady-state solutions are sought, the system is solved in a transient manner to increase the stability of imposing the body force components, which, in the transient solution, have a more gradual effect on the development of the wake, yet converge to a steady-state solution. Both spatial and temporal discretization is first-order accurate. Spatially, the mesh is kept very refined to minimize the spatial discretization error. The temporal accuracy is of less importance as the solution approaches steady state. User-defined functions are employed to incorporate the body forces (3.22) as source terms in the actuator disc region, with $\Omega = 1$ rad s^{-1}. Apart from the symmetry axis, the boundary conditions for the domain are given by a (slip) wall boundary condition at $r = 25\delta$, preventing any flow entering or leaving the domain in the radial direction. The inflow condition, upstream of the disc, is defined as a pressure inlet condition with a gauge total pressure of 0.5 Pa. As outlet condition, a target mass flow of 1963.495 kg s^{-1} is prescribed, which translates to an unperturbed flow velocity of $U_0 = 1$ m s^{-1}, as the density is equal to 1 kg m^{-3}. From an initial, uniform solution field, the simulation is run for 1200 time steps with a time step of 1 s, which develops the flow field under the influence of the imposed actuator disc source terms.

B.2. *Rotor calculations in* § 4

B.2.1. *Vortex panel code*

The three-dimensional unsteady potential flow panel model is described in detail in Micallef (2012). The code is used to simulate the behaviour of time-dependent motions of bodies such as wind turbine blades using a number of suitable boundary conditions. The formulation used for this work is based on that proposed by Katz & Plotkin (1991); the general procedure is given here. The bodies are discretized into panel elements of sources and doublets. The kinematic motion of the bodies is determined and can be represented in general by a translation and a rotation of the following form:

$$\frac{\partial \varPhi}{\partial n} = (\boldsymbol{U}_0 + \boldsymbol{v}_{rot} + \boldsymbol{\varOmega} \times \boldsymbol{r}) \boldsymbol{\cdot} \boldsymbol{n}, \tag{B 1}$$

where $\varPhi$ is the potential function, and $\boldsymbol{n}$ is the normal direction to a surface. As the blades rotate, new wake panels are shed from the trailing edge. For this wake shedding process, the Kutta condition must hold. Thus, for the vorticity at the trailing edge to be zero, one must have

$$\mu_{Wt} = (\mu_u - \mu_l)_t, \tag{B 2}$$

where W refers to the wake, u to the upper surface of the blade, l to the lower surface, t is the time, and μ represents the doublet strength. This shedding process is repeated every time step. The panel model uses a Dirichlet boundary condition. This can then be used to evaluate the velocities by means of differentiating the potential function,

$$\nabla \varPhi = -\frac{1}{4\pi} \int_{S_B} \sigma \nabla \left(\frac{1}{x}\right) \mathrm{d}s + \frac{1}{4\pi} \int_{S_B+S_W} \mu \nabla \left[\frac{\partial}{\partial n} \left(\frac{1}{x}\right)\right] \mathrm{d}S + \nabla \varPhi_0, \tag{B 3}$$

where x is the distance from the panel to a point P in the flow field, S_B represents the body surface, S_W represents the wake surface and σ is the source strength.

The body source and doublet distributions are hence computed numerically from

$$\sum_{k=1}^{N} C_k \mu_k + \sum_{i=1}^{N_w} C_i \mu_i + \sum_{k=1}^{N} B_k \sigma_k = 0, \tag{B 4}$$

where the summation from 1 to N represents the addition over all body panels, and the summation from 1 to N_w represents the addition over all wake panels. This will enable the wake strength to be determined for every time step. Also, for each time step, the velocity at each panel vertex must be calculated. This enables the estimation of the displacement of each wake vertex using a first-order Euler time-marching approximation. This allows the wake to evolve freely under the influence of the free stream and wake inductions.

For the panel model simulation, the grid convergence index (GCI) parameter (see Roache 1998) is adapted for use in assessing the convergence of a solution in a vortex-based approach. Grid independence and convergence of test quantities are considered. The GCI is defined as

$$\mathrm{GCI}(\%) = \frac{|\epsilon|\eta^p}{\eta^p - 1} \times 100, \tag{B 5}$$

where η is the ratio of the total number of panels with respect to a reference simulation while p is the order of the numerical method used (here taken as one since the method uses a first-order time-marching scheme). The error estimator ϵ is defined as

$$\epsilon = \frac{f - f_{ref}}{f_{ref}}, \tag{B 6}$$

where f is the variable on which the convergence is being assessed and f_{ref} is the value of that variable from a reference simulation (with an extremely fine discretization). To assess discretization convergence, a number of simulations based on a coarser body and wake panel distribution were run. The mesh independence results show bound vorticity at different radial stations. With increasing number of body elements, the GCI falls below 2.5 %. The convergence for the very fine case is also assessed on the basis of the number of revolutions of the turbine. In these simulations, 10 revolutions are used. Results are shown for axial inductions at $r/R = 0.5$ and different x/R. The convergence of maximum bound vorticity is also shown. Again, the results converge to within 2.5 %, which is considered sufficient for these simulations.

B.2.2. *CFD code*

The CFD results were computed with the open-source C++ object-oriented numerical toolbox OpenFOAM using a Reynolds-averaged Navier–Stokes simulation approach (OpenFOAM 2013). OpenFOAM is a finite-volume software for solving numerically partial differential equations. The computation was run in parallel in the FLOW computer cluster of the University of Oldenburg using 180 cores. An unstructured and hexa-dominant mesh design was chosen for its high adaptability (in comparison to structured meshes) to complex geometries. The computational mesh includes both blades and the nacelle. The tower is omitted, since it is assumed that it does not significantly influence the aerodynamic phenomena studied in this work. More than 99 % of the mesh elements are hexahedra, the rest being polyhedra. The total number of cells is 20 million. For the actuator line simulations, the same kind of grid was used, but the number of cells could be reduced to 4 million owing to the fact that no turbine components were meshed. The whole mesh generation process has been carried out with tools available in OpenFOAM. The comparatively low computational cost of the actuator line model allowed a time-accurate computation to be performed, whereas a steady-state simulation was used for the full rotor approach. In that case, the rotation of the rotor was accounted for by adding the Coriolis and centrifugal forces to the momentum equations in the regions subjected to rotation. This avoided the use of computationally expensive moving grids. The pressure–velocity coupling was accomplished by means of the SIMPLE algorithm in the full rotor case and by the PIMPLE algorithm in the actuator line case. The Prandtl/Glauert tip loss correction (see Glauert 1935, chapter VII) has been applied to the computation with the actuator line to obtain a more realistic loading both at the blade tip and root. An available actuator line library from NREL (2013) was used for implementing an in-house solver for that kind of computation. In both types of simulations, a second-order linear upwind discretization scheme has been used for the convective terms. The simulations were run fully turbulent using the turbulence model by Spalart & Allmaras (1994). This turbulence model has been chosen for its robustness and satisfactory performance for wall-bounded and adverse-pressure-gradient flows, as well as for its comparatively low sensitivity to grid resolution. In spite of its limitations for separated and wake flows, it is well suited for the research presented here considering blade loads at attached flow conditions. The calculation of the forces has been accomplished in two different ways: integrating the surface pressure along the blade walls, and applying the Kutta–Joukowsky theorem

	$T_{\varphi,blade}$	$T_{x,blade}$	$T_{\varphi,tip}$	$T_{x,tip}$	$R/T_{x,tip}$
GCI	0.75	1.16	0.35	0.02	0.13

TABLE 2. Discretization error of the CFD simulations.

to the circulation obtained after 'probing' the wind speed field at a distance of 5 mm around the blade surface. The velocity component tangential to the blade surface was used to derive the radial vorticity, whereas the chordwise vorticity was derived from the radial velocity component. The radial circulation was obtained by integrating the radial vorticity from the leading to the trailing edge. The chordwise circulation was computed by integrating the chordwise vorticity from inboard radial positions towards the blade tip.

The uncertainty of the CFD simulations has been assessed by means of the GCI (Roache 1998). Simulations with a coarse, medium and fine grid have been performed using 10×10^6, 15×10^6 and 20×10^6 cells, respectively. In order to achieve convergence, the residuals for all the field variables were monitored to ensure a residual decrease of at least three orders of magnitude. Furthermore, the integral quantities torque and thrust were also monitored during the simulation for convergence. Starting with the 10×10^6 cells grid, the mesh has been systematically refined, i.e. the refinement itself was structured in spite of the mesh being of type unstructured. The obtained results, summarized in table 1, refer to the finest mesh, which is the one from which the CFD results presented in this article have been extracted. The study of the numerical uncertainty has been done focusing first on the azimuthal load per blade, $T_{\varphi,blade}$, and thrust per blade, $T_{x,blade}$. The corresponding levels of uncertainty presented in table 2 are sufficiently low to consider this general verification of the simulation model as satisfactory. Further, the uncertainty in the tip region of the blade, which is the main region of interest for the research, is analysed in more detail. Table 2 gives the uncertainty for the thrust force $T_{x,tip}$ associated with the outer 10 % of the blade span, the radial force $\mathscr{R}$ as well as the ratio $\mathscr{R}/T_{x,tip}$. This force ratio $\mathscr{R}/T_{x,tip}$ is ≈10 %, i.e. ≈80 times higher than its corresponding uncertainty, so the uncertainty of the simulation model is considered to be low enough for the scope of our study.

B.3. *Experiments in* § *4*

The SPIV experiments for the TU Delft rotor B were carried out in the Open Jet Facility (OJF) wind tunnel at TU Delft. The wind tunnel has an octagonal jet exit with a 3 m equivalent diameter. The test section measures 6 m × 6.5 m × 13.5 m. The jet diameter is large enough to permit at least 2 m diameter rotors to be tested with minimal effects on blockage. The entire flow field was measured along the blade spanwise and chordwise directions. Wake measurements were also carried out at various blade angles such that the full three-dimensional wake structure can be visualized. Measurements were carried out for axial flow as well as yawed flow.

The OJF, the SPIV technique and measurement campaigns are described in Micallef *et al.* (2011, 2013). The rotational speed of the TUD-B rotor model has the same orientation as indicated in figure 4. The chord c and twist θ of the blade tip of the model rotor vary from $c=0.107R, \theta=1.4^\circ$ at $r=0.8R$ to $c=0.098R, \theta=0^\circ$ at the tip, so the chord line of the tip aerofoil is purely azimuthal. The tip has a flat cut-off tip surface. The results presented in this paper concern the rotor operating at its optimal tip speed ratio of seven at a wind speed of 6 m s^{-1}.

In § 4.3.3 the radial load is determined by a momentum balance as described in del Campo *et al.* (2013), where it is applied to determine the load on the radial circulation. Application of the integral momentum conservation concept permits the integral forces acting on the body to be computed from their reaction on the flow, without the need to explicitly evaluate the flow quantities at the surface of the model. The momentum balance is applied in the rotating coordinate system with the centrifugal and Coriolis forces accounted for. Viscous and turbulent stresses are neglected, as they do not play a significant role when the integration contour is at a sufficient distance from the body. The velocity is known from the SPIV measurements, and the pressure at the right-hand side is determined by (3.12) written as $\boldsymbol{\nabla} p = -(\boldsymbol{v}_{rot} \boldsymbol{\cdot} \boldsymbol{\nabla})\boldsymbol{v}_{rot} + \boldsymbol{v}_{rot} \times 2\boldsymbol{\Omega} - \boldsymbol{\Omega} \times (\boldsymbol{\Omega} \times \boldsymbol{e}_r r)$.

REFERENCES

AKAY, B., SIMÃO FERREIRA, C. J., VAN BUSSEL, G. J. W. & HERRAEZ, I. 2012 Experimental and numerical quantification of radial flow in the root region of a HAWT. In *Proceedings 50th AIAA Aerospace Sciences Meeting, Nashville, TN. AIAA Paper* 2012-0896. Available at: http://repository.tudelft.nl/.

BATCHELOR, G. K. 1970 *An Introduction to Fluid Dynamics*. Cambridge University Press.

BETZ, A. 1919 Schraubenpropeller mit geringstem Energieverlust. Dissertation. *Göttinger Nachrichten*. Göttingen.

BETZ, A. 1920 Das Maximum der theoretisch möglichen Ausnützung des Windes durch Windmotoren. *Z. Gesamte Turbinenwesen* **26**, 307–309.

BRAGG, S. L. & HAWTHORNE, W. R. 1950 Some exact solutions of the flow through annual cascade actuator discs. *J. Aeronaut. Sci.* **17**, 243–249.

BRESLIN, J. P. & ANDERSEN, P. 1994 *Hydrodynamics of Ship Propellers*. Cambridge University Press.

BURTON, T., SHARPE, D., JENKINS, N. & BOSSANYI, E. 2001 *The Wind Energy Handbook*. John Wiley & Sons.

DEL CAMPO, V., RAGNI, D., MICALLEF, D., DIEZ, F. J. & SIMAO FERREIRA, C. 2013 3D Load estimation on a horizontal axis wind turbine using SPIV. *Wind Energy* (published online); doi:10.1002/we.1658.

CONWAY, J. T. 1995 Analytical solutions for the actuator disk with variable radial distribution of load. *J. Fluid Mech.* **297**, 327–355.

CONWAY, J. T. 1998 Exact actuator disc solutions for non-uniform heavy loading and slipstream contraction. *J. Fluid Mech.* **365**, 235–267.

FERRER, E. & MUNDUATE, X. 2007 Wind turbine blade tip comparison using CFD. *J. Phys.: Conf. Ser.* **75**, 012005.

FROUDE, R. E. 1889 On the part played in propulsion by differences of fluid pressure. *Trans. Inst. Nav. Archit.* **30**, 390–405.

GLAUERT, H. 1926 *The Analysis of Experimental Results in the Windmill Brake and Vortex Ring States of an Airscrew*. Aeronautical Research Committee, Reports and Memoranda, vol. 1026. H.M. Stationery Office.

GLAUERT, H. 1935 The general momentum theory. In *Aerodynamic Theory* (ed. W. F. Durand), Volume IV, Division L. Springer. (Reprinted 1963 Dover).

GOLDSTEIN, S. 1929 On the vortex theory of the screw propeller. *Proc. R. Soc. Lond.* A **123**, 440–465.

GREY, R. B., MCMAHON, H. M., SHENOY, K. R. & HANIMER, M. L. 1980 Surface pressure measurement at two tips of a model helicopter rotor in hover. *NACA Tech. Rep.* CR-3281.

GREENBERG, M. D. 1972 Nonlinear actuator disc theory. *Z. Flugwiss.* **20** (3), 90–98.

HAND, M. M., SIMMS, D. A., FINGERSH, L. J., JAGER, D. W., COTRELL, J. R., SCHRECK, S. & LARWOOD, S. M. 2001 Unsteady aerodynamics experiment phase VI: wind tunnel test configurations and available data campaigns. *Tech Rep.* NREL/TP-500-29955. National Renewable Energy Laboratory.

HERRAEZ, I., MEDJROUBI, W., STOEVESANDT, B. & PEINKE, J. 2012 Aerodynamic simulation of the MEXICO rotor. In *Proceedings of the Science of Making Torque from Wind, J. Phys.: Conf. Ser.* (in press).

HORLOCK, J. H. 1978 *Actuator Disk Theory*. McGraw-Hill.

JOUKOWSKY, N. E. 1912–1918 Four papers in vortex theory of screw propeller. In *Théorie Tourbillonnaire de l'Hélice Propulsive*, Gauthier-Villars, 1929, (French translation from Russian).

JOUKOWSKY, N. E. 1918 Fourth paper in *Transactions of the Office for Aerodynamic Calculations and Essays of the Superior Technical School of Moscow*, 1918 (in Russian). Also published (in French) in *Théorie Tourbillonnaire de l'Hélice Propulsive*, Quatrième Mémoire. Gauthier-Villars, 1929.

JOUKOWSKY, N. E. 1920 Windmill of the NEJ type. In *Transactions of the Central Institute for Aero-Hydrodynamics of Moscow*. Also published in: *Collected Papers*, Vol. VI. Joukowsky Institute for AeroHydrodynamics, 1937 (in Russian).

VON KÁRMÁN, TH. & BURGERS, J. M. 1935 Motion of a perfect fluid produced by external forces. In *Aerodynamic Theory* (ed. W. F. Durand), Volume II, Division E, chap. IIIA. Springer. (Reprinted 1963 Dover).

KATZ, J. & PLOTKIN, A. 1991 *Low-Speed Aerodynamics*. McGraw-Hill.

KŰCHEMANN, D. 1984 *The Aerodynamic Design of Aircraft*. Pergamon.

VAN KUIK, G. A. M. 1991 On the limitations of Froude's actuator disc concept. PhD thesis, Technical University Eindhoven, The Netherlands.

VAN KUIK, G. A. M. 2007 The Lanchester–Betz–Joukowsky limit. *Wind Energy* **10**, 289–291.

VAN KUIK, G. A. M. 2012 The relationship between loads and power of a rotor and an actuator disc. In *Proceedings of the Science of Making Torque from Wind, J. Phys.: Conf. Ser.* (in press).

VAN KUIK, G. A. M. 2014 On the generation of vorticity in rotor and disc flows. On the generation of vorticity by force fields in rotor and actuator flows. *Renew. Energy* (published online); http://dx.doi.org/10.1016/j.renene.2014.02.056.

VAN KUIK, G. A. M. & VAN ZUYLEN, A. H. 2009 On actuator disc force fields generating wake vorticity. *Abstracts of Euromech Symposium 508 on Wind Turbine Wakes, Madrid*, pp. 26–28.

KUNDU, P. K. 1990 *Fluid Mechanics*. Academic Press.

LANCHESTER, F. W. 1915 A contribution to the theory of propulsion and the screw propeller. *Trans. Inst. Nav. Archit.* **57**, 98–116.

LEISHMAN, J. G. 2000 *Principles of Helicopter Aerodynamics*. Cambridge University Press.

LIGHTHILL, J. 1986 *An Informal Introduction to Fluid Mechanics*. Clarendon Press.

MADSEN, H. A., BAK, C., DØSSING, M., MIKKELSEN, R. & ØYE, S. 2010 Validation and modification of the blade element momentum theory based on comparisons with actuator disc simulations. *Wind Energy* **13**, 373–389.

MANWELL, J. F., MCGOWAN, J. G. & ROGERS, A. L. 2007 *Wind Energy Explained*. John Wiley & Sons.

MICALLEF, D. 2012 3D flows near a HAWT rotor: a dissection of blade and wake contributions. PhD thesis, TU-Delft/University of Malta. Available at: http://repository.tudelft.nl/.

MICALLEF, D., AKAY, B., SANT, T., SIMÃO FERREIRA, C. & VAN BUSSEL, G. 2011 Experimental and numerical study of radial flow and its contribution to wake development of a HAWT. *Proc. EWEA 2011 Conference, Brussels, 14–17 March*. EWEA. Available at: http://www.ewea.org/annual2011/conference/conference-proceedings/.

MICALLEF, D., AKAY, B., SIMÃO FERREIRA, C., SANT, T. & VAN BUSSEL, G. 2012 The origins of a wind turbine tip vortex. In *Proceedings of the Science of Making Torque from Wind, J. Phys.: Conf. Ser.* (in press).

Micallef, D., van Bussel, G., Simão Ferreira, C. & Sant, T. 2013 An investigation of radial velocities for a horizontal axis wind turbine in axial and yawed flows. *Wind Energy* **16**, 529–544.

Mikkelsen, R., Øye, S., Sørensen, J. N., Madsen, H. A. & Shen, W. Z. 2009 Analysis of wake expansion and induction near tip. *Proc. EWEC09, Marseille, France*. Available at: http://proceedings.ewea.org/ewec2009/proceedings/index.php?page=zip.

Milne-Thomson, L. M. 1966 *Theoretical Aerodynamics*. 4th edn Macmillan, (Reprinted 1973 Dover).

NREL 2013 Computer-aided engineering tools: SOWFA. http://wind.nrel.gov/designcodes/simulators/sowfa/ last visited January 2014.

Okulov, V. L. & Sørensen, J. N. 2010 Maximum efficiency of wind turbine rotors using Joukowsky and Betz approaches. *J. Fluid Mech.* **649**, 497–508.

Okulov, V. L. & van Kuik, G. A. M. 2012 The Betz–Joukowsky limit: on the contribution to rotor aerodynamics by the British, German and Russian scientific schools. *Wind Energy* **15**, 335–344.

OpenFOAM 2013 OpenFOAM: The open source CFD toolbox. www.openfoam.com last visited January 2014.

Øye, S. 1990 A simple vortex model. *Proceedings of 3rd IEA Symposium on the Aerodynamics of Wind Turbines, ETSU, Harwell*, pp. 4.1–5.15.

Prandtl, L. 1918 Tragflügeltheorie I Mitteilung. *Nachr. Ges. Wiss. Göttingen Math. Phys. Kl.* 451–477.

Ragni, D., van Oudheusden, B. W. & Scarano, F. 2011 Non-intrusive aerodynamic loads analysis of an aircraft propeller blade. *Exp. Fluids* **51**, 361–371.

Ragni, D., van Oudheusden, B. W. & Scarano, F. 2012 3D pressure imaging of an aircraft propeller blade-tip flow by phase-locked stereoscopic PIV. *Exp. Fluids* **52**, 463–477.

Rankine, W. J. M. 1865 On the mechanical principles of the action of propellers. *Trans. Inst. Nav. Archit.* **6**, 13–39.

Réthoré, P., van der Laan, P., Troldborg, N., Zahle, F. & Sørensen, N. N. 2014 Verification and validation of an actuator disc model. *Wind Energy* **17**, 919–937.

Roache, P. J. 1998 *Verification and Validation in Computational Science and Engineering*. Hermosa.

Rosen, A. & Gur, O. 2008 Novel approach to axisymmetric actuator disk modelling. *AIAA J.* **46**, 2914–2925.

Saffman, P. G. 1992 *Vortex Dynamics*, Cambridge Monographs on Mechanics and Applied Mathematics. Cambridge University Press.

Sanderse, B., van der Pijl, S. P. & Koren, B. 2011 Review of computational fluid dynamics for wind turbine wake aerodynamics. *Wind Energy* **14**, 799–819.

Schepers, J. G., Boorsma, K. & Munduate, X. 2012 Final results from Mexnext-I: analysis of detailed aerodynamic measurements on a 4.5 m diameter rotor placed in the large German Dutch Wind Tunnel DNW. In *Proceedings of the Science of Making Torque from Wind, J. Phys.: Conf. Ser.* (in press).

Schepers, J. G. & Snel, H. 2007 Model experiments in controlled conditions (MEXICO). *ECN Report* ECN-E-07–042.

Shen, W. Z., Mikkelsen, R., Sørensen, J. N. & Bak, C. 2005 Tip loss corrections for wind turbine computations. *Wind Energy* **8**, 457–475.

Shen, W. Z., Zhu, W. J. & Sørensen, J. N. 2012 Actuator line/Navier–Stokes computations for the MEXICO rotor: comparison with detailed measurements. *Wind Energy* **15**, 811–825.

Shives, M. & Crawford, C. 2013 Mesh and load distribution requirements for actuator line CFD simulations. *Wind Energy* **16**, 1138–1196.

Sibuet Watters, C. & Masson, C. 2010 Application of the actuator surface concept to wind turbine rotor aerodynamics. *Wind Energy* **13**, 433–447.

Sørensen, J. N. & Shen, W. Z. 2002 Numerical modelling of wind turbine wakes. *Trans. ASME: J. Fluids Engng* **124**, 393–399.

Sørensen, J. N., Shen, W. Z. & Munduate, X. 1998 Analysis of wake states by a full-field actuator disc model. *Wind Energy* **1**, 73–88.

SØRENSEN, J. N. & VAN KUIK, G. A. M. 2011 General momentum theory for wind turbines at low tip speed ratios. *Wind Energy* **14**, 821–839.

SPALART, P. R. 2003 On the simple actuator disc. *J. Fluid Mech.* **494**, 399–405.

SPALART, P. R. & ALLMARAS, S. R. 1994 A one-equation turbulence model for aerodynamic flows. *Rech. Aéronaut.* **1** (1), 5–21.

THWAITES, B. 1960 *Incompressible Aerodynamics*. Clarendon Press.

TROLDBORG, N., SØRENSEN, J. N. & MIKKELSEN, R. 2010 Numerical simulations of wake characteristics of a wind turbine in uniform inflow. *Wind Energy* **13**, 86–99.

DE VRIES, O. 1979 *Fluid Dynamic Aspects of Wind Energy Conversion*, AGARDograph, vol. 243. AGARD.

WALD, Q. R. 2006 The aerodynamics of propellers. *Prog. Aerosp. Sci.* **42** (2), 85–128.

WU, T. Y. 1962 Flow through a heavily loaded actuator disc. *Schiffstechnik* **9** (47), 134–138.

XIAO, J., WU, J., CHEN, L. & SHI, Z. 2011 Particle image velocimetry (PIV) measurements of tip vortex wake structure of wind turbine. *Appl. Math. Mech.* **32** (6), 729–738.